Isotopic composition of convective rainfall in the inland tropics of Brazil

Vinicius dos Santos[1], Didier Gastmans[1], Ana María Durán-Quesada[2], Ricardo Sánchez-Murillo[3], Kazimierz Rozanski[4], Oliver Kracht[5] and Demilson de Assis Quintão[6].

[1]São Paulo State University (UNESP), Environmental Studies Center. Av. 24ABased, 1515, Bela Vista, 13.506-900, Rio Claro, São Paulo, Brazil. vinicius.santos16@unesp.br; didier.gastmans@unesp.br

[2]Escuela de Física & Centro de Investigación en Contaminación Ambiental & Centro de Investigaciones Geofísicas, Universidad de Costa Rica, San José 11501, Costa Rica. ana.duranquesada@ucr.ac.cr

[3]University of Texas at Arlington, Department of Earth and Environmental Sciences, 500 Yates Street, Arlington, Texas 76019, USA. ricardo.sanchezmurrillo@uta.edu

[4]Faculty of Physics and Applied Computer Science, AGH University of Krakow, al. Mickiewicza 30, 30-059 Krakow, Poland. rozanski@agh.edu.pl

[5]International Atomic Energy Agency, Isotope Hydrology Section, Vienna International Centre, P. O. Box 100, 1400 Vienna, Austria. O.Kracht@iaea.org

[6]São Paulo State University (UNESP), IPMet/Science College, Est. Mun. José Sandrin IPMET, S/N, 17.048-699, Bauru, São Paulo, Brazil. demilson.quintao@unesp.br

Correspondence to: Didier Gastmans (didier.gastmans@unesp.br)

Abstract. Strong convective systems characterize theThe tropical central-southern region of Brazil. is characterized by strong convective systems. These systems provide abundant water supply for agro-industrial activities andbut also pose flood risks to large cities. Here, we present high-frequency (2-10 min; inter and intra-event) rainfall isotopic compositions (n=90 samples) to reveal the regional and local atmospheric processes controlling the isotopic variability of convective systems betweenfrom 2019-2021. Inter- . Isotope parameters from individual events rainfall weighted-average (δ_{wgd}) values were low ($\delta^{18}O_{wgd} \leq$ -10.0 ‰) due to , including initial ($\delta_{initial}$), median (δ_{med}), and the influence of evapotranspiration from the Amazon forest during the summer anddifference between lowest and highest isotope values ($\Delta\delta$), and detailed meteorological data, were used in inter-event and intra-event analysis. The lower $\delta_{initial}$ values were associated with higher rainfall along Hysplit trajectories. In contrast, from the Amazon forest during the summer, compared to autumn and spring seasons, when Hysplit trajectories from the Atlantic Ocean and South Brazil exhibitedhad lower rainfall amounts, resulting in high $\delta^{18}O_{wgd} \geq$ -4.2 ‰. of rainfall. Consequently, there were high $\delta_{initial}$ values. This strong regional δ_{wgd} pattern often masks δ signature was conserved during certain convective intra-event isotopic variability. Therefore, we analyzedevents, with similar values between the $\delta_{initial}$ and δ_{median}. However, for other intra-events, the $\delta_{initial}$ values were altered by local processes connected to cloud features, rainfall vertical structure of local rainfall, and humidity conditions, resulting in increased isotopic variations ($\Delta\delta$) during intra-events.

Our analysis includes inter and intra-event evaluations. For inter-event analysis, use rainfall weighted-average (δ_{wgd}) values. These values were more negative ($\delta^{18}O_{wgd} \leq -10.0$ ‰) due to evapotranspiration from the Amazon forest during the summer. This was associated with higher rainfall along Hysplit trajectories, compared to autumn and spring. During these seasons, Hysplit trajectories from the Atlantic Ocean and South Brazil had lower amounts of rainfall, resulting in high $\delta^{18}O_{wgd} \geq -4.2$ ‰. This regional δ-signature masked the local processes analysed in the intra-event analysis. The local rainfall is affected by its vertical structure, which can be measured using reflectivity (Z) from micro radar data.parameters (maximum, median and amplitude) in the vertical profile of the MRR. Variations in Z indicate thatchanges in isotopic patterns caused by microphysical processes within falling of raindrops ledduring their fall to changes in $\delta^{18}O$ and *d*-excessthe surface. Our findings establish a novel framework for evaluating the meteorological controls on the isotopic variability of convective precipitation in tropical South America, fill the gap of high-frequency studies in this region, and generate ana comprehensive isotopic meteorological dataset for convectivefuture model evaluations.ing evaluation studies.

Formatado: Subscrito

Formatado: Sobrescrito

Formatado: Subscrito

Formatado: Sobrescrito

Formatado: Subscrito

1 Introduction

The tropical central-southern region of Brazil (CSB) is the primary contributor to the country's economy, with agriculture and agroindustry as the main sectors (Zilli et al., 2017). These economic activities are highly dependent on seasonal rainfall for irrigation and hydropower supply (Luiz Silva et al., 2019). Projected changes in the frequency of heavy and extreme rainfall events in future climate scenarios (Marengo et al., 2020; Donat et al., 2013; IPCC, 2021; Marengo et al., 2021) pose a significant threat to regional economic growthenterprises and energypower generation. Similarly, according to Marengo et al. (2021), simulations with the pre-CMIP6 models suggest that the intensification of heavy rainfall events could exacerbate the prevalence of floods and landslides in susceptible regions. Such occurrences have resulted in a total cost of US$41.7 billion over the past half-century (Marengo et al., 2020; World Meteorological Organization, 2021).

Extreme precipitation events are linked to convective systems (CS). These systemsThe CS significantly contribute to the proportion of annual rainfall budget and account for a large numbersignificant portion of extreme rainfall events (Roca and Fiolleau, 2020). Across the tropics, diurnal surface heating amplifies convection, generating short-lived events that can occur in consecutive days. Rapid upward movement of air results in large condensation and precipitation rates quick condensation and formation of precipitation with substantial droplets and heavy rainfall (Breugem et al., 2020; Kastman et al., 2017; Lima et al., 2010; Machado et al., 1998). This is identified by vigorous vertical development in the form of *cumulus-nimbus* and *cumulus congestus* (convective clouds) and low-level divergence (stratiform clouds) (Siqueira et al., 2005; Machado and Rossow, 1993; Zilli et al., 2017; Houze, 1989, 2004). Precipitation associated with these systems are commonly referred as convective and stratiform rainfall, and account for 45% and 46% of the total rainfall in South America, respectively (Romatschke and Houze, 2013).

Whether rainfall is convective or stratiform rainfall has been suggested to determine variations in stable isotope composition of precipitation across the tropics (Zwart et al., 2018; Sánchez-Murillo et al., 2019; Sun et al., 2019; Han et al., 2021; Aggarwal et al., 2016; Munksgaard et al., 2019). Processes driving the variations in the isotopic composition in CSconvective systems are more complex and less understood compared to the case of other precipitation producing systems. (de Vries et al., 2022). Studies using the isotopic composition of rain and water vapor have quantified and modelled physical processes related to convection (Bony et al., 2008; Kurita, 2013). Previous studies have suggested that the isotopic composition of CSconvective systems is connected to the integrated history of convective activity (Risi et al., 2008; Moerman et al., 2013), depth of organized convection and aggregation (Lawrence et al., 2004; Lekshmy et al., 2014; Lacour et al., 2018; Galewsky et al., 2023), microphysical processes within clouds (Aggarwal et al., 2016; Lawrence et al., 2004; Zwart et al., 2018), and cold pool dynamics (Torri, 2021). These interpretations simplified and lumped the effects of multiple rainfall timescales (e.g. monthly, daily and sub-hourlyhigh frequency), providing different perspectives on convective processes, such as the regional (synoptic forcings) and local factors (e. g. microphysical processes occurring both within and below the cloud) (Kurita et al., 2009; Muller et al., 2015; Graf et al., 2019; Lee and Fung, 2008)...

Processes driving the variations in the isotopic composition in convective systems are more complex and less understood compared to the case of other precipitation producing systems (de Vries et al., 2022). Studies using the isotopic composition of rain and water vapor have quantified and modelled physical processes related to convection (Bony et al., 2008; Kurita, 2013). Previous studies have suggested that the isotopic composition of convective systems is connected to the integrated history of convective activity (Risi et al., 2008; Moerman et al., 2013), depth of organized convection and aggregation (Lawrence et al., 2004; Lekshmy et al., 2014; Lacour et al., 2018; Galewsky et al., 2023), microphysical processes within clouds (Aggarwal et al., 2016; Lawrence et al., 2004; Zwart et al., 2018), and cold pool dynamics (Torri, 2021). These interpretations simplified and lumped the effects of multiple rainfall timescales (e.g. monthly, daily and high frequency), providing different perspectives on convective processes, such as the regional (synoptic forcings) and local factors (e. g. microphysical processes occurring both within and below the cloud) (Kurita et al., 2009; Muller et al., 2015).

High-frequency rainfall sampling and analyses of stable isotope ratios has been used to better understand the evolution of large weather systems such as tropical cyclones and typhoons (Sun et al., 2022; Sánchez-Murillo et al., 2019; Han et al., 2021), squall lines (Taupin et al., 1997; Risi et al., 2010; Tremoy et al., 2014; de Vries et al., 2022), and mid-latitude cyclones, and cold fronts (Barras and Simmonds, 2009; Celle-Jeanton et al., 2004; Aemisegger et al., 2015; Thurnherr and Aemisegger, 2022; Muller et al., 2015; Landais et al., 2023). High-resolution isotope information can provide a better insight into the(Barras and Simmonds, 2009; Celle-Jeanton et al., 2004; Aemisegger et al., 2015; Thurnherr and Aemisegger, 2022; Landais et al., 2023; Muller et al., 2015). local evaporation effects (Graf et al., 2019; Aemisegger et al., 2015; Lee and Fung, 2008). High-resolution isotope information can provide a better insight into the development of weather systems and cloud dynamics, both responsible for changes in the rain type, intensity, and inherent isotope isotopic variability during the life cycle of rainfall events (Coplen et al., 2008; Muller et al., 2015; Celle-Jeanton et al., 2004).

In this study, we used high-frequency rainfall sampling to disentangleinvestigate regional (moisture origin/transport, regional atmospheric circulation) fromand local (below-cloud processes, vertical structure of rainfall, cloud top temperature) processes that controlling the isotopic composition of convective rainfall. High-frequency rainfall was integrated with ground-

Código de campo alterado

Código de campo alterado

Código de campo alterado

based observational data (Micro Rain Radar and automatic weather station), satellite imagery (GOES-16), ERA-5 reanalysis products, and HYSPLIT trajectories to better characterize convective rainfall over the inland tropics of Brazil.

2 Data and Methods

2.1 Sampling site and weather systems

The rainfall sampling site was located~~localized~~ in Rio Claro city, São Paulo State (Fig. 1a). The station (-22.39°S, -47.54°W, 670 m a.s.l.) is part of the Global Network of Isotopes in Precipitation network (GNIP) and is influenced by weather systems responsible for rainfall variations and seasonality linked to the regional atmospheric circulations across the CSB region. The rainfall seasonality over CSB is associated with: (i) frontal systems (FS), represented mainly by cold fronts from southern South America acting throughout the year, and (ii) the activity of the South Atlantic Convergence Zone (SACZ) during austral summer (December to March) (Kodama, 1992; Garreaud, 2000) (Fig. 1b). These features are mostly responsible for CS development (Romatschke and Houze, 2013; Siqueira et al., 2005; Machado and Rossow, 1993) (Fig. 1c), and were captured during their passage over the Rio Claro station.

2.2 Rainfall sampling and isotope analyses

High-frequency rainfall sampling was conducted using a passive collector (2 to10 minutes intervals) from September 2019 to February 2021, except for April, July, and August (during winter 2020), when no rainfall was observed in the study area. The pandemic Covid-19 disrupted access to the university campus, thereby reducing the number of rainfall events sampled during the spring of 2020, particularly at night (e.g., lockdowns). In this study, the rainfall samples collected do not consist of consecutive day-night pairs during the same day. In total, 90 samples representing eight convective events (3 night-time and 5 day-time events) were collected. Samples were transferred to the laboratory and stored in 20 mL HDPE bottles at 4ºC~~4 ºC~~. In parallel to high-frequency sampling, monthly cumulative rainfall samples were also collected~~ at the Rio Claro site during the study period as a contribution to the GNIP network,~~ using the methodology recommended by the International Atomic Energy Agency (IAEA, 2014).

Rainfall samples were analyzed for stable isotope composition using Off-Axis Integrated Cavity Output Spectroscopy (Los Gatos Research Inc.) at the Hydrogeology and Hydrochemistry laboratory of UNESP's Department of Applied Geology and at the Chemistry School of the National University (UNA, Heredia, Costa Rica). All results are expressed in per mil relative to Vienna Standard Mean Ocean Water (V-SMOW). The certified calibration standards used in UNESP were USGS-45 (δ^2H = −10.3 ‰, $\delta^{18}O$ = −2.24 ‰), USGS-46 (δ^2H = −236.0 ‰, $\delta^{18}O$ = −29.80 ‰), including one internal standard (Cachoeira de Emas - CE – δ^2H = −36.1 ‰, $\delta^{18}O$ = −5.36 ‰). USGS standards were used to calibrate the results on the V-SMOW2-SLAP2 scale, whereas CE was used for memory and drift corrections. At UNA, the certified standards MTW (δ^2H = −130.3 ‰, $\delta^{18}O$

= −16.7 ‰), USGS45 (δ^2H = −10.3 ‰, δ^{18}O = −2.2 ‰), and CAS (δ^2H = −64.3 ‰, δ^{18}O = −8.3 ‰) were used to correct the measurement results for memory and drift effects and to calibrate them on the V-SMOW2-SLAP2 scale (García-Santos et al., 2022). The analytical uncertainty (1σ) was 1.2 ‰ for δ^2H and 0.2 ‰ for δ^{18}O for UNESP analysis and 0.38 ‰ for δ^2H and 0.07 ‰ for δ^{18}O for UNA analysis. Deuterium excess (*d*-excess) was calculated as: *d*-excess = δ^2H - 8*δ^{18}O (Dansgaard, 1964), with uncertainties (1σ) of 1.33 and 0.43 ‰, respectively. This secondary isotope parameter was used to interpret the influence of moisture origin/transport (Sánchez-Murillo et al., 2017; Froehlich et al., 2002) and local processes (Aemisegger et al., 2015; Muller et al., 2015; Celle-Jeanton et al., 2004).

2.3 Meteorological data

An Automatic Weather Station (AWS) Decagon Em50 (METER) was installed next to~~near~~ the Micro Rain Radar (MRR) (METEK) at 670 m.a.s.l, within~~in~~ immediate vicinity of the rainfall collection site. Meteorological data were recorded at 1 min intervals for rain rate (RR, mm min^{-1}), air temperature (T, °C) and relative humidity (RH, %). The MRR data for reflectivity (Z, in~~Ze,~~ dBZ), and fall velocity (w, m s^{-1}) were also recorded at 1 min intervals. MRR parameters correspond to the mean values measured at the elevation between 150 and 350 meters above surface. MRR operated at a frequency of 24.230 GHz, modulation of 0.5 – 15 MHz according to the height resolution mode. For this work, different height resolutions (31 range bin) were tested, 150 m, 200 m, 300 m and 350 m, resulting in vertical profiles of 4650 m, 6200 m, 930 0m and 10.850 m, respectively (Endries et al., 2018). The MRR data used in the following discussion are the near-surface data (first measurement from 150 m to 350 m). Lifting Condensation Level (LCL, meters) was computed from AWS RH and T, using expression proposed by Soderberg et al. (2013). The~~) and~~ rainfall amount (R, mm) was also calculated during the sampling interval. GOES-16 imagery was used to identify the convective nuclei of the cloud-top (10.35-μm, Band-13) and brightness temperature (BT, °C), at 10 min intervals during the sampling period (Ribeiro et al., 2019; Schmit et al., 2017). The 10.35-μm BT is often used to estimate the convective cloud depth, since the lower BT is linked to deeper cloud tops (Adler and Fenn, 1979; Roberts and Rutledge, 2003; Adler and Mack, 1986; Ribeiro et al., 2019; Machado et al., 1998). The weather systems (fronts, instabilities, and low pressure) were defined according to the synoptic chart and meteorological technical bulletin of the Center for Weather Forecast and Climatic Studies of the National Institute of Space Research (CPTEC/INPE) that used information of numerical models, automatic weather stations, satellite and radar images, reanalysis data and regional atmospheric models, such as the Brazilian Global Atmospheric Model and ETA model.

2.4 Hysplit modeling and Reanalysis data

The origin of air masses and moisture transport to the Rio Claro site were evaluated using the HYSPLIT (Hybrid-Single Particle Langragian Integrated Trajectory) modeling framework (Stein et al., 2015; Soderberg et al., 2013). The trajectories of the air masses were estimated for 240 hours prior to rainfall onset, considering the estimated time of residence of the water vapor (Gimeno et al., 2010, 2020; van der Ent and Tuinenburg, 2017). Start time of trajectories was the same as the start time of rainfall events. The trajectories were computed using NOAA′s meteorological data (global data assimilation system, GDAS: 1 degree, global, 2006-present), with ending elevations of the trajectories at 1500 m above the surface, taking into account the climatological height of the Low Level Jet, within 1000–2000 m (Marengo et al., 2004). Ten-day trajectories representing convective events were calculated as trajectory ensembles, each consisting of twenty-seven ensemble members released at start hour of convective rainfall sample collection. Ensembles were produced by varying the initial trajectory wind speeds and pressures, according to the HYSPLIT ensemble algorithm, in order to account for the uncertainties involved in the simulation of individual backward trajectories (Jeelani et al., 2018). A sum of the rainfall intensity (mm hr^{-1}) along the trajectories was used to analyse rainout of the moist air masses according to the Jeelani et al. (2018).

Reanalysis data were used to better understand the influence of atmospheric circulation on isotopic composition of rainfall at the study area. ERA-5 information was used to evaluate hourly vertical integrals of eastward water vapor flux (kg m^{-1} s^{-1}) during convective events sampled. The Global Modeling and Assimilation Office (GMAO) data (MERRA-2, 1 hour, 0.5 x 0.625 degree, V5.12.4 were used for calculations of latent heat flux (LHF). Aqua/AIRS L3 Daily Standard Physical Retrieval (AIRS-only) data (1-degree x 1-degree V7.0, Greenbelt, MD, USA, Goddard Earth Sciences Data and Information Services Center) (known as GES DISC) were used for average outgoing longwave radiation (OLR). OLR values below 240 W m^{-2} indicate organized deep convection (Gadgil, 2003).

2.5 Identification of convective rainfall events and vertical variations of reflectivity

In general, the identification of CS~~convective precipitation systems~~ was based on the vertical structure of the given precipitation system (lack of the melting layer and bright band - BB) in the radar profiles featuring high reflectivity values (Z~~Zc~~ > 38 dBZ) (Houze, 1993, 1997; Steiner and Smith, 1998; Rao et al., 2008; Mehta et al., 2020; Endries et al., 2018) and satellite imagery (Vila et al., 2008; Ribeiro et al., 2019; Siqueira et al., 2005; Machado et al., 1998). Consequently, ~~convective rainfall was defined in this study by (i)~~ convective ~~rainfall was defined in this study by (i) convective~~ cloud nuclei observed in GOES-16 imagery, (ii) no BB detected, (iii) Z~~Zc~~ > 38 dBZ near to the surface and (iv) rainfall intensity (AWS) of at least 10 mm h^{-1} (Klaassen, 1988) (Fig. 1c,d). The convective nuclei were identified using GOES-16 imagery, determined as a contiguous area of at least 40 pixels with BT lower than 235K (≤ -38 °C) over Rio Claro station, according to previous studies (Ribeiro et al., 2019).

The Z is defined as the mean number of raindrops within a specific diameter interval per unit volume of air. Therefore, Z represents the concentration of a particular raindrop property (in this case, the 6^{th} power of their diameter, proportional to the square of their volume) (Houze, 1993; Mehta et al., 2020; Uijlenhoet, 2001). A highhigher Z value indicates a highhigher concentration of raindrops. A modification in the formation mechanism for precipitation particles results in a change in Z of the vertical profile (Houze, 1997). Descriptive statistics were conducted on the Z values at different heights to comprehend and quantify the dynamics of rain particle formation during intra-events. The resulting parameters from considering the entire vertical profile of the MRR are: Z_{max}Zmáx: is the maximum reflectivity value in the vertical profile indicating the maximum

Formatado: Espanhol (Espanha), Verificar ortografia e gramática

Formatado: Espanhol (Espanha)

Código de campo alterado

Formatado: Sobrescrito

concentration of raindrops; Z_{median}: refers to the median reflectivity in the vertical profile and was used to synthetize the change in vertical Z values; and $Z_{amplitude}$ (Z_{ampl}): is defined as the difference between the maximum and minimum reflectivity values in the vertical profile. In other words, asimpler terms, the larger Z_{ampl} indicates that raindrops undergo the Z amplitude, the more microphysical transformations the raindrops undergo as they fall to the surface.

Formatado: Subscrito

Formatado: Subscrito

2.6 Preliminary assessment of local processes

Below-cloud atmospheric conditions are known to be relevant and while we acknowledge that a more robust dataset is required to provide sound conclusions, a preliminary assessment of this factor is herein included.

Since the isotopic composition of near-ground water vapor during the rainfall events was not measured, the framework proposed by Graf et al. (2019) for interpreting below-cloud effects on rainfall isotopes cannot be applied here. A semi-quantitative evaluation of those effects is demonstrated for all rainfall events, despite the need for a more substantial dataset to establish firm conclusions. This analysis considers the following assumptions: (i) median values of isotope and meteorological parameters recorded for each analysed event (Table 1) will be used in the calculations, (ii) linear interpolation of air temperature and relative humidity between the cloud base level and the ground level will be adopted to estimate the relative humidity at the cloud base (RH_{INT}), (iii) it will be assumed that atmosphere is saturated with water vapour at the cloud base level (RH = 100 %), and (iv) the reservoir of water vapour below the cloud base level is isotopically homogeneous (Risi et al., 2019; Sarkar et al., 2023).

Isotopic evolution of raindrops falling through unsaturated humid atmosphere beneath the cloud base level will be calculated using the generally accepted conceptual framework for isotope effects accompanying evaporation of water into a humid atmosphere (Craig and Gordon, 1965; Horita et al., 2008). Isotopic evolution of an isolated water body (e.g. falling raindrop) evaporating into a humid atmosphere can be described by the following equations (Gonfiantini, 1986):

$$\delta = \left(\delta_o - \frac{A}{B}\right) F^B + \frac{A}{B} \qquad (1)$$

where

$$A = \frac{h_N \delta_A + \varepsilon_{kin} + \varepsilon_{eq}/\alpha_{eq}}{1 - h_N + \varepsilon_{kin}} \qquad (2)$$

and

$$B = \frac{h_N - \varepsilon_{kin} - \varepsilon_{eq}/\alpha_{eq}}{1 - h_N + \varepsilon_{kin}} \qquad (3)$$

Parameter F describes the remaining fraction of the evaporating mass of water (raindrop), while δ_A stands for the isotopic composition of ambient moisture. Initial and actual isotopic compositions of the evaporating water body, expressed in δ notation, are represented by δ_o and δ, respectively. The variables in equations (3) and (4) are described as:

h_N – relative humidity of the ambient atmosphere, normalized to the temperature of the evaporating water body;

α_{eq} – temperature-dependent equilibrium fractionation factor, derived from empirical equations proposed by Horita and Wesolowski (1994);

ε_{eq} – equilibrium fractionation coefficient: $\varepsilon_{eq} = \alpha_{eq} - 1$ (4)

ε_{kin} – kinetic fractionation coefficient; $\varepsilon_{kin} = \alpha_{kin} - 1$ (5)

The kinetic fractionation coefficient is a linear function of the relative humidity deficit in the ambient atmosphere (Gat, 2001; Horita et al., 2008):

$$\varepsilon_{kin} = n \cdot \varepsilon_{diff}(1 - h_N) \quad (6)$$

where n describes a turbulence parameter, varying from zero to one and ε_{diff} is the kinetic fractionation coefficient associated with diffusion of water isotopologues in air.

The value of n is controlled mainly by wind conditions prevailing over the evaporating surface. It quantifies the apparent reduction of ε_{diff} due to the impact of turbulent transport. The value of $n = 0.5$, was adopted in the calculations, following the results of laboratory experiments with evaporation of water drops in a humid atmosphere reported by Stewart (1975). Following this same publication, the value of the F parameter for each event was computed based on the rate of change of evaporated drop radius as a function of ambient relative humidity (Stewart, 1975). Droplets with a drop size distribution of 1mm are assumed based on previous studies in this region of study (Zawadzki and Antonio, 1988; Cecchini et al., 2014). Travel time of raindrops drops from the cloud base to the surface was derived from the position of LCL level and the terminal velocity of drops. It was further assumed in the calculations that the difference between drop temperature and ambient air temperature is small, thus allowing to use ambient humidity instead to normalized humidity. Although this assumption may result in an over-estimation of the impact of partial evaporation of raindrops on their isotope characteristics, the effect is expected to be small due to high ambient relative humidities (> 90 %) used in the calculations.

2.67 Statistical tests

The Shapiro-Wilk test was applied to verify that the data distribution was normal (parametric) or non-normal (non-parametric) (Shapiro, S. S.; Wilk, 1965). A significant difference (p-value < 0.05) indicates a non-parametric distribution. A Spearman rank correlation test was used for nonparametric distribution data, whereas Pearson's linear correlation test was applied for parametric data. Correlation tests were conducted between isotopes ($\delta^{18}O$ and *d*-excess) and meteorological data (AWS and MRR variables) during the same time interval and from individual events. Correlation tests were not applied to GOES-16 BT and reanalysis data due to their temporal resolution, which reduced the number of samples. All tests were performed with significance levels defined by a p-value < 0.05, using the R statistical package (R Core Team, 2023).

To explore the vertical variation of Zc values measured by the MRR, we carried out descriptive statistics, including minimum, maximum, amplitude, mean, standard deviation, and arithmetic mean. Rainfall weighted averages were also calculated, for each event to evaluate large-scale processes using the equation:

$$\delta_{wgd} = \frac{\sum_{i=1}^{n} Ri\delta i}{\sum_{i=1}^{n} Ri} \qquad (1)$$

where δ_{wgd} is the rainfall weighted average of the isotopic composition, R_i is the rainfall of the event (mm), δ_i is the isotopic composition of an individual sample (‰), and n is the number of samples from each event. Rainfall weighted averages refers to the $\delta^{18}O_{wgd}$, $\delta^{2}H_{wgd}$ and d_{wgd}, and median of the $\delta^{18}O_{med}$, $\delta^{2}H_{med}$ and d_{med}.

~~A statistical analysis was carried out to characterize regional and local influences, in accordance with He et al. (2018). The initial isotope data of the events ($\delta_{initial}$) closely reflects the initial air mass or vapor from which the precipitation originates. The $\delta_{initial}$ and median (δ_{med}) values were employed to identify regional influences in inter-event analysis. Also, the difference ($\Delta\delta$) between the lowest $\delta^{18}O$ and the highest $\delta^{18}O$ value represents the local change in δ-value during the intra-event (Muller et al., 2015; He et al., 2018).~~

~~3~~ 3 Results

3.1 Inter-event variability of meteorological and isotopic parameters ~~and synoptic characteristics~~

3.3.1. Seasonal-mean climatic and isotopic conditions

~~3.1~~

The isotopic composition of monthly rainfall exhibits clear seasonal variations between September 2019 and February 2021 (Fig. 2a). Seasonal variability was characterized by wet (low $\delta^{18}O$) and dry (high $\delta^{18}O$) seasons (austral summer and autumn-spring, respectively). Summer~~High-frequency sampling of convective events could not be done uniformly during the study period, but it is still evident that median $\delta^{18}O$ values of high-frequency sampling events (black symbols in Fig. 2a) follow the seasonal isotope variability.~~

~~The summer~~ months were characterized by the influence of convective activity, reflected in high latent heat flux and lower OLR (Fig. 2 b-d~~2c~~). During autumn and spring, significant lower latent heat flux and higher OLR were associated with less convective development (Houze, 1997, 1989). The formation of convective rainfall may not be primarily controlled by diurnal thermal convection, as rainfall is more likely to be associated with frontal systems (Siqueira and Machado, 2004), as observed in the rainfall episodes during autumn and spring.

A significant influence of the cold fronts was observed before, during, and after their passage over the study area (Fig. 2a). During autumn and spring, the convective events of 2019/11/05, 2020/11/18, and 2020/05/23 were associated with cold fronts in the study area. On 2020/06/09, changes in the regional atmosphere over the state of São Paulo caused convective rainfall

Formatado: Subscrito

Formatado: Subscrito

Formatado: Fonte: Negrito

Formatado: Fonte: Negrito

Formatado: Normal, Sem marcadores ou numeração

Formatado: Recuo: Primeira linha: 0 cm due to an instability (frontal) system resulting from a cold front settling over the southern region of Brazil. During the summer season, convective rainfall also occurred on 2020/02/01 and 2021/02/24 due to cold fronts and instability (frontal), respectively. In addition, the thermal convection over land ~~of the continental region caused atmospheric ascent via surface heating in the inland of Brazil~~, lead ~~ing~~ to ~~a system responsible for the~~ convective rainfall event on 2020/01/30. As a result of the interaction between thermal convection and the incursion of the frontal system, a low-pressure system (frontal) was responsible for the convective rainfall event on 2020/02/10.

3.3.2. Isotopic and local meteorological variations

Table 1 presents an overview of the sampling, isotope compositions (δ~~parameters (~~~~$\delta_{initial}$,~~ δ_{med} (median)~~,~~ and ~~Δ~~δ_{wgd}) and median values of meteorological variables from individual events. The ~~Sampled events had a~~ duration of sampled events ranged from 141 min to 18 min.~~or fewer minutes.~~ The T and T_{wd} exhibited small differences among the events. In contrast, RR, RH, LCL, Z~~Ze~~, w, and BT varied considerably between events. The maximum recorded values for these parameters were 97 %, 489 m, 46 dBZ, 8 m s^{-1} and -63 °C, respectively.

Isotope values varied among convective events, with a range of -11.0 ‰, -91.2~~92.8~~ ‰ and +15.7 ‰ for $\delta^{18}O_{med}$, $\delta^{2}H_{med}$~~median values of $\delta^{18}O$, $\delta^{2}H$~~ and d_{med}~~*d*-excess~~, respectively. In most cases, the median and weighted average of $\delta^{18}O$, $\delta^{2}H$ and *d*-excess have similar and equal values. However, there is one event where the median for *d*-excess is 7.2 and the weighted average is 11.1 (Table 1). ~~The maximum differences between the $\delta_{initial}$ and δ_{med} for $\delta^{18}O$, $\delta^{2}H$, and *d*-excess were 1.6 ‰, 9.1 ‰, and 9.5 ‰, respectively. The maximum Δδ values for all isotopes parameters, $\delta^{18}O$, $\delta^{2}H$ and *d*-excess were 7.3 ‰, 43.0 ‰ and 19.2 ‰, respectively.~~

3.1.3. ~~32. Inter-event variability of the isotope parameters~~ Moisture origin

~~Hysplit air mass back-trajectories revealed three main locations as moisture origin during the presence of convective rainfall: Amazon forest, Atlantic Ocean, and southern Brazil (Fig. 3).~~ The sourcing of moisture for rainfall over Rio Claro varies seasonally and spatially, suggesting complex interactions in moisture transport and mixing that strongly influence the δ_{wgd} ~~initial~~ isotopic composition of rainfall throughout the year (Table 1). Hysplit air mass back-trajectories revealed three main domains as moisture origin during the presence of convective rainfall: Amazon forest, Atlantic Ocean, and southern Brazil (Fig. 3).

Summer rainfall events were characterized by the trajectory and length of moist air masses arriving from the Amazon forest (2020/02/10, 2020/02/01, and 2020/01/30) (Fig. 3a). As a result, there was a large amount of rainfall along Hysplit trajectories. Rainfall amounts were 177 mm, 126 mm and 78 mm, respectively.~~, for these dates.~~ Remarkably, these events exhibited ~~very~~ similar isotope characteristics ($\delta^{2}H_{wgd}$, $\delta^{18}O_{wgd}$~~$\delta^{2}H_{wgdinitial}$, $\delta^{18}O_{wgdinitial}$~~) (Table 1). In contrast, the event on 2021/02/24 presented

Formatado: Subscrito

Formatado: Sobrescrito

Formatado: Sobrescrito

Formatado: Fonte: Itálico

Formatado: Fonte: Itálico

higher $\delta_{wgdwgdinitial}$ values, reflecting the oceanic moisture influence (Fig. 3a), with a lowest amount of rainfall (53 mm) along Hysplit trajectory.

Based on ERA-5, the vertically integrated eastward vapor flux corroborates the influence of a distinct mechanism for moisture transport and $\delta_{wgdwgdinitial}$ values. Negative values for vertical vapor fluxes over the Amazon forest during sampled convective events in summer (Fig. 4a, b, d) clearly illustrate a westward moisture flux from the Atlantic Ocean to the Amazon forest. Positive values in the central-southern region of Brazil indicate moisture being transported eastward from the Amazon forest. However, these moisture fluxes were not observed on 2021/02/24 when the eastward vapor flux was positive with high values over the Atlantic Ocean (250 ~ 750 kg m^{-1} s^{-1}).

The autumn convective events on 2020/05/23 and 2020/06/09 revealed a significant continental origin of moist air masses (from south-western Brazil). In addition, during the second event, the Amazon-type trajectory started in the southern Atlantic and did not reach the boundary of the rainforest (Fig. 3b). BothIn both autumn events reported, there was the lowest amount of rainfall amounts (4 mm) along Hysplit trajectories. On 2020/05/23 negative vertical flux values (-500 ~ -250 kg m^{-1}s^{-1}) were observed in south-western Brazil, indicating moisture transport from the Atlantic Ocean to the continent. This favored a vapor flux (500 ~ 750 kg m^{-1}s^{-1}) from western Brazil to the study area (Figure 4f). On 2020/06/09, there were slightly negative values (-250 ~ 0 kg m^{-1}s^{-1}) of eastward vapor flux in the Amazon forest, indicating less influence from rainforest moisture. Conversely, positive vapor flux values (250 ~ 500 kg m^{-1}s^{-1}) were observed in the western part of continental Brazil.

Two events in the spring season (Fig. 3c) also showed contrasting origin of moisture and d_{wgd}initial weighted average *d*-excess values, despite only slight differences in $\delta^{18}O_{wgd}$ $^{18}O_{wgdinitial}$ (Table 1). The mean trajectory on 2020/11/18 clearly belongs to the Amazon category, although it only passed over the south-eastern boundary of the Amazon rainforest and had a much shorter length and lower rainfall along Hysplit trajectory (23 mm) compared to the Amazon trajectories observed during the summer season. Thus, positive values of the eastward vapor flux (250 ~ 750 kg m^{-1} s^{-1}) were not distributed along the Amazon forest to the Atlantic Ocean as typically observed (Fig. 4h). The mean trajectory on 2019/11/05 the eastward vapor flux (> 500 kg m^{-1} s^{-1}, Fig. 4g) were circling around Rio Claro, indicating the continental moisture origin (from southern Brazil), and low amount of rainfall along Hysplit trajectory of 8 mm.

3.223 Intra-event variability of the isotope and meteorological parameters

The temporal evolution of isotope characteristics and selected meteorological parameters of convective rainfall are shown in Fig. 5--6 (summer), and Fig. 776 (autumn) and Fig. 8 (-(spring). The vertical Z variation of the MRR in all events shows a pattern of values ranging from 0 to 10 dBZ at the top, a wide band of lowest values and noise attenuating the reflectivity producing white horizontal and vertical bands, and an increase in Z values closer to the surface where ZmaxZmáx occurs (highest values ranging from 44 to 51 dBZ). During intra-events, Z, isotopic parameters, and GOES-16 BT display distinct temporal patterns across events and seasons. There are largewide variations in ZZc values and inverse, opposite patterns of variation between δ^{18}O and *d*-excess (much more variable), and between T and RH. Different decreasing, increasing or stable trendsColder BT values were observed in BT values.and decrease or stable during intra-events, which did not occurs for R. The key meteorological component of each event is detailed the following sections described the main seasonal results for . The study emphasizes the intra-lack of pattern in the measured values for reflectivity (Zc) in the vertical profile. Only higher Zc values were observed near the surface (from 2km to 200m), which indicates an increase in rain rates. Despite the similar vertical structure, the temporal evolution varied considerably among events. Furthermore, the GOES-16 BT shows unique temporal patterns among events.

The differences in Δδ observed between convective events were explained by intra-events (refer to Table 1) and how local factors may affect the regional isotopic signature as illustrated by the inter-event analysis.

3.223.1. During summer sSummer intra-events

Low variability patterns were observed on 2020/02/01 (Fig. 5, left) and 2020/01/30 (Fig. 5, right) for δ^{18}O, T, RH, and BT. Both events were shorter in duration (≤ 25 minutes) and had a higher R (≤ 5.4 mm) value at the beginning, which decreased over the course of the event (0.2 mm). Similar patterns of MRR vertical profiles were observedprofile occurred between the events, illustrated by similar Z valuesparameters, with low variability of Zmedian (7 ~ 17 dBZ and 8 ~ 15 dBZ), ZmaxZmáx (23 ~ 48 dBZ and 19 ~ 46 dBZ) and ZZc amplitude decreasing along the event (17 ~ 45 dBZ and 19 ~ 42 dBZ), respectively. StrongThe strong and significant ($p < 0.0001$) correlations were observed between isotopic composition and MRR parameters for 2020/02/01: δ^{18}O-ZZc (r = -0.9), δ^{18}O-w (r = -0.9), δ^{18}O-Zmáx (r = -0.9), δ^{18}O-Zampl (r = -0.8), *d*-excess-ZZc (r = 0.9), and *d*-excess-w (r = 0.9), *d*-excess-ZmaxZmáx (r = -.9) and *d*-excess-Zampl (r = 0.9). No), while there were no significant correlations between isotopic composition and meteorological parameters for 2020/01/30, except foralthough a moderate correlation was observed between δ^{2}H and Zmedian (r = -0.5).

Formatado: Recuo: Primeira linha: 0 cm

Large isotopic and meteorological variations were observed for 2021/02/24 (δ^{18}O: -7.9 ~ -4.4 ‰, *d*-excess: +1.2 to +18.4 ‰) and 2020/02/10 (δ^{18}O: -15.2 ~ -7.9 ‰, *d*-excess: +4.8 ~ +21.4 ‰.) (Fig.‰.). Nevertheless, for both events there were no possible defined isotopic pattern variations characterized by specific abrupt changes corresponding to variations of R and Z parameters (grey bands in Fig. 6). On 2021/02/24 a strong and significant ($p < 0.05$) correlation was observed between δ^{18}O and R (r = -0.8), Z (r = -0.6), ZmaxZmáx (r = -0.6), Zampl (r = -0. 6), Zmedian (r = 0.7), and between *d*-excess and R (r = -0.6), Z (r = -0.5), ZmaxZmáx (r = 0.5), Zampl (r = 0.5) and Zmedian (r = -0.7). For 2020/02/10, the significant correlations were reportedcorrelation was between δ^{18}O-RH (r = -0.5), *d*-excess-RH (r = 0.5) and *d*-excess and Zmedian (r = 0.5).

In addition, *d*-excess values lower than +10 ‰ were observed at the end of the events (2020/02/01, 2020/02/10 and 2021/02/24),, corresponding to low values of the R and Z parameters and high RH (black dotted cycle in Figs.Figures 5 and 6).

Lower values of $\Delta\delta^{18}O$ were observed on the 2020/02/01 and 2020/01/30 compared to higher $\Delta\delta^{18}O$ values observed on the 2020/02/10 and 2021/02/24. In contrast, all summer events exhibit high Δδ values for *d*-excess (Table 1). Despite this variation in isotopic amplitude, the evolution of these events is characterized by different amounts of available humidity (Table 1 and Table 2). For the 2021/02/24 event, lower humidity values were observed below the cloud (RH_{INT} = 93 %) and at the surface (RH 78 ~ 88 %, median value 86 %). The other events had higher humidity conditions (RH_{INT} = > 96 % and RH > 90 %). Nevertheless, only 2021/02/24 and 2020/02/10 show d-excess values lower than 10 ‰, suggesting that the specific local factors can influence the variations in the isotopic composition of the precipitation, as shown below for each event.

Specifically, the events on 2020/02/01 (Fig. 5c,e) and 2020/01/30 (Fig. 5d,f) showed consistent $\delta^{18}O$ trends (-11.6 ~ -10.0 ‰ and -10.6 ~ -9.6 ‰, respectively). In contrast, these events showed an inverted V-shaped (from 11.3 ~ 15.3 ‰ to 15.4 ~ 7.0‰) and V-shaped (from 20.8 ~ 11.4 ‰ to 14.6 ~ 16.2 ‰) patterns for *d*-excess, respectively. The patterns of rainfall intensity were similar for both events, with high rainfall amount at the beginning of event, decreasing over the time. In BT values, decreased (-50 ~ -65 °C) and constant variations (-52 ~ -53 °C) occurred on 2020/02/01 and 2020/01/30 events, respectively. The strong and significant ($p < 0.0001$) correlations were observed between isotopic composition and MRR parameters for 2020/02/01: $\delta^{18}O$-Zc (r = -0.9), $\delta^{18}O$-w (r = -0.9), *d*-excess-Zc (r = 0.9) and *d*-excess-w (r = 0.9), while there were no correlations between isotopic composition and meteorological parameters for 2020/01/30.

On 2021/02/24 (Fig. 5i,k) and 2020/02/10 (Fig. 5j,l), notable fluctuations were observed in both the isotope and meteorological parameters. On 2021/02/24, $\delta^{18}O$ varied from -7.9 ~ -4.4 ‰, and *d*-excess varied from 1.2 to 18.4 ‰. The evolution of the event was characterized by varying local weather conditions, as evidenced by a larger BT range (-38 ~ -57 °C). Radar reflectivity is displayed in a vertical profile, illustrating these changes, with larger Zc values during the event (red colors in Fig. 5g). As a result, three peaks of maximum rainfall amount were observed, which corresponded to the distinct $\delta^{18}O$ and for *d*-excess values: at 15:49 local time (2.6 mm, -7.6‰ and 13.0 ‰), at 16:24 (3.1 mm, -6.9 ‰ and 8.4 ‰) and at 17:28 (3.3 mm, -7.9 ‰ and 17.9 ‰), respectively. Also, strong, and significant ($p < 0.05$) correlation was observed between $\delta^{18}O$-R (r = -0.8), *d*-excess-R (r = -0.6) and MRR parameter, $\delta^{18}O$-Zc (r = -0.6) and *d*-excess-Zc (r = -0.5).

On 2020/02/10, $\delta^{18}O$ showed a variation from -15.2 ~ -7.9 ‰ and for *d*-excess from 4.8 ~ 21.4 ‰. During the beginning of the event and until 21:03 local time, high BT values (-16 ~ -45 °C) corresponded to the higher Zc values (red colors in Fig. 5h) and high RH (~ 97 %). After this time, lower Zc and lowest BT values were observed (-45 ~ -57 °C). There were two breakpoints in the rainfall trend (increasing to decreasing) corresponding to the change in isotope values ($\delta^{18}O$ and *d*-excess), occurring at 20:36 (4.8 to 3.2 mm, -13.9 to -9.5 ‰ and 15.7 to 9.4 ‰) and 21:57 (2.0 to 0.8 mm, -14.9 to -7.9 ‰ and 21.4 to 4.8‰) respectively. In addition, for this event strong and significant ($p < 0.05$) correlation was observed only between $\delta^{18}O$-RH (r = -0.5) and *d*-excess-RH (r = 0.5).

Formatado: Recuo: Primeira linha: 0 cm

3.23.2.2 During autumnaAutumn and spring intra-events

AutumnThe autumn events show distinct isotopic patterns. of variation. The 2020/05/23 event exhibitedhad a small isotopic ($\delta^{18}O$: -2.6 ~ -2.7 ‰, *d*-excess: +16.7 ~ +19.0 ‰) and meteorological (declining T, R and Z parameters along the event) variation (Fig.Figure 7). On 2020/06/09 (Fig.Figure 7) two isotopic distribution patterns were recorded,occurred, the first with minimalshort variation ($\delta^{18}O$: -3.6 ~ -3.4 ‰, *d*-excess: +26.4 ~ +17.7 ‰) and large (the second with high $\delta^{18}O$: -values (-1.5 ~ -2.9 ‰;‰) and low *d*-excess: + (+15.3 ~ +6.3 ‰) variations, corresponding to high RH, R, Zamplt and ZmaxZmáx (grey bands in Fig. 8). Strong and significant ($p < 0.05$) correlations were observed between $\delta^{18}O$-RH (r = 0.5), $\delta^{18}O$-T (r = -0.6), *d*-excess-RH (r = -0.6), *d*-excess-T (r = 0.7) and *d*-excess- Zamplt (r = -0.5) on 2020/06/09. However, no significant correlations were found during the event on 2020/05/23.

DistinctiveSpring events exhibit unique isotopic patterns were also found during spring events.of variation. On 2019/11/05, a change in the vertical profile and Z parameters was observed (grey bands in Fig. 8), with a shift in $\delta^{18}O$ from maximum depletion (-4.1 ‰) to enrichment at the end of the event (-3.2 ~ -1.7 ‰). On 2020/11/18, (Fig. 8), there was a gradual decrease observed in $\delta^{18}O$ (-2.7 ~ -5.4 ‰) and an increase in *d*-excess (+10.2 ~ +23.1 ‰). The latter‰) observed during the event. This was accompanied by a progressive increase in RH, decrease in T, and constant values of Zmedian values (Fig. 87b, d, f, h, j). On 2019/11/05 a strong and significant ($p < 0.005$) correlations werecorrelation was observed between $\delta^{18}O$ and Z (r = -0.7), w (r = -0.7), ZmaxZmáx (r = -0.7) and Zampl (r = -0. 6), and between *d*-excess and RH (r = -0.7), T (r = 0.8), w (r = 0.6), Zampl (r = 0.5) and Zmedian (r = -0.5). For 2020/11/18, the significant correlations were obtainedcorrelation was between $\delta^{18}O$-RH (r = -0.5), $\delta^{18}O$-T (r = 0.7), *d*-excess-Zampl (r = 0.7).

Lower $\Delta\delta^{18}O$ values were observed during autumn and spring events in comparison to summer events. Both autumn and spring events showed higher $\Delta\delta$ values for *d*-excess when compared to summer events. For the events on 2020/05/23 (RH_{INT} = 93 %, RH 78 ~ 89 %, with median of 87 %) and 2020/11/18 (RH_{INT} = 92 % and RH 70 ~ 90 %, with median of 85 %), lower humidity conditions were recorded, whereas for all other events, humidity conditions were high (RH_{INT} = > 97 % and RH = > 90%) as show in Tables 1 and 2.

For autumn events on 2020/06/09 (Fig. 6a,c,e) and 2020/05/23 (Fig. 6b,d,f), a slight increase trend (-3.7 ~ -1.5‰) and stationary trend (-2.6 ~ -2.7‰) were observed regarding $\delta^{18}O$. On the other hand, for the same events, *d*-excess showed a W-shaped trend (17.7 ~ 6.3 ‰, during the last part of the event) and V-shaped pattern (16.7 ~ 19.0 ‰), respectively. Both events demonstrated a decrease in rainfall amount: from 6.2 to 0.2 mm on 2020/06/09, 2020, and from 2.6 to 0.2 mm on 2020/05/23. Additionally, the range of BT increased from -55°C to -35 °C and from -60°C to -52 °C, respectively. Strong and significant ($p < 0.05$) correlations were observed between isotopic and surface meteorological parameters during the event on 2020/06/09, $\delta^{18}O$-RH (r = 0.5), $\delta^{18}O$-T (r = -0.6), *d*-excess-RH (r = -0.6), and *d*-excess-T (r = 0.7). However, no significant correlations were found during the event on 2020/05/23.

Spring convective events exhibited contrasting variations in isotopes and meteorological conditions. On 2019/11/05 (Fig. 6g,i,k), slight fluctuations were observed in $\delta^{18}O$ (-3.0 ~ -1.7 ‰, slightly increasing trend), while *d*-excess values were higher

~~(21.0 ~ 28.0 ‰, decreasing trend). This slight fluctuations in $\delta^{18}O$ values correspond to the constant and higher Zc near surface. This is evidenced by the highest and significant ($p < 0.0003$) correlations observed between isotopic and MRR parameters, $\delta^{18}O$-Zc (r = -0.7), $\delta^{18}O$-w (r = -0.7), and *d*-excess-w (r = 0.6). In contrast, these fluctuations were not related with changes in rainfall amount (0.6 ~ 5.0 mm) and BT (-65 ~ -62 °C).~~

~~On 2020/11/18, two distinct steps revealed a decreasing trend in $\delta^{18}O$ (-2.7 ~ -5.4 ‰), and a substantial increasing trend in *d*-excess (10.2 ~ 23.1 ‰) (Fig. 6h,j,l). Between 15:10 and 16:05 local time, the vertical profile of the MRR exhibited variable Zc values, with concomitant decreases in both BT values (-62 and -65 °C) and $\delta^{18}O$ (-2.7 ~ -4.0 ‰) and increase in both rainfall (1.2 ~ 2.0 mm), *d*-excess (10.2 ~ 19.6 ‰) and RH (70 ~ 82 %) values. After this period, Zc values increased closer to the surface, resulting in a slight decrease in temperature (-65 ~ -63 °C). Additionally, $\delta^{18}O$, *d*-excess, rainfall amount and RH fluctuated (-3.8 ~ -5.4 ‰, 18.0 ~ 23.1 ‰, 1.8 ~ 2.2 mm and 84 ~ 90 %, respectively). Regardless of this, no significant correlations were found due to the considerable variations between isotopic and rainfall, as well as BT and MRR parameters. The significant ($p < 0.001$) correlations were only observed for $\delta^{18}O$-RH (r = -0.9), $\delta^{18}O$-T (r = 0.9), *d*-excess-RH (r = 0.9), and *d*-excess-T (r = -0.9).~~

4. Discussion

DetailedDescription ~~tailed~~ evaluations of the isotopic variability in convective rainfall werewas ~~ere~~ provided atat~~by~~ both inter- and intra-event scales. The key regional and local controls on the isotopic composition of convective rainfall can be divided in two groups: (i) rainfall produced by different moisture source region(s) represented by ~~s~~cale~~. Such separation between inter-~~event isotopic values, and (ii) local effects associated with vertical rainfall structure and surface meteorological conditions. In ~~and intra-events allows for improved evaluation of fractionation processes that occurred during moisture transport towards the formation of local rainfall. Generally~~ In general~~, during~~ the summer, thermal conditions dominate convective processes. During~~, while during~~ autumn and spring, convective rainfall was~~is~~ associated with frontal systems (Fig. 2). In this regard. δ_{wgd}~~It is crucial to q~~ Q~~uantify these synoptic variations~~ is crucial ~~t~~f~~o~~r ~~understand~~ing ~~seasonal differences in atmospheric conditions, which~~ that ~~affect~~ the ~~moisture source and transport across seasons. Th~~e~~us, the~~ δ_{wgd}~~initial~~ values better constrainedcapture the large-scale processes (such as vaporvapour origin, convective activity and weather systems) with stronger due to the ponderation by rainfall amount dependencies. The individual isotopic , reducing the local effects, for example illustrated by the increase in *d*-excess value on 2021/02/24 (arithmetic mean of +7.2 ‰)and weighted-average of +11.1 ‰) (Table 1). The patterns of isotopic variations are more influenced by local effects revealed microphysical processes such as coalescence (i.e., higher concentration of raindrops with high Z values) hat are often masked, revealing processes that are hidden by weighted averages and long-term averages during the evolution of individual precipitation systems. ~~are influenced by vapor origin, convective activity, and weather systems, which may be further modified by local processes, resulting in distinct values of δ_{med} and large $\Delta\delta$.~~

Formatado: Recuo: Primeira linha: 0.5 cm

Formatado: Fonte: Itálico

~~Th~~us, ~~e~~ the ~~key regional and local controls o~~n~~f the isotopic composition of convective rainfall are, respectively: (i) rainfall of~~rom ~~moist air masses during their transport in the atmosphere, from the source region(s) to the collection site showed by inter-event analysis, and (ii) local effects associated with convective cloud characteristics, vertical rainfall structure and near-surface~~ meteorological ~~humidity conditions.~~

4.1 Regional atmospheric controls

Regional aspects of atmospheric moisture transport to ~~the~~ Rio Claro ~~site~~ were illustrated in HYSPLIT backward trajectories (Fig. 3) and maps of vertically integrated moisture flux across~~in~~ the region (Fig. 4). Most of moist air masses arriving at Rio Claro during summer ~~(2020/02/10, 2020/02/01, and 2020/01/30)~~ exhibited a common origin in the equatorial Atlantic Ocean and were subjected to a long rainfall rainout~~of moist air masses~~, extending over several thousand kilometers. Along this pathway, air masses interacted with the Amazon forest. Intensive moisture recycling resulted in~~of moisture leads to~~ a small continental isotope gradient ~~of δ-values of rainfall~~ across the Amazon forest (Salati et al., 1979; Rozanski et al., 1993) and elevated *d*-excess (Gat, J. R., & Matsui, 1991). At Rio Claro, the arriving air masses are depleted in heavy isotopes (δ_{wgdwgd}~~$_{initial}$~~ ≤ -10.0 ‰) due to rainout~~enhanced amount of rainfall~~ along the trajectories (≥ 78 mm), ~~after the southeastern deflection from the Andes,~~ with consistent d_{wgd} > +14~~initial~~ weighted average ~~*d*-excess higher than +1~~4~~0~~.0 ‰, inherited through the interaction of maritime moisture with the Amazon forest. In contrast, the summer event on 2021/02/24 was influenced by oceanic moisture and had a short trajectory compared to ~~the~~ other typical summer events. ~~, as indicated by the lower amount of rainfall along the Hysplit trajectory (53 mm), which explains the higher~~ ~~δ_{wgd}~~~~$_{initial}$~~ ~~values ($\delta^{18}O$ = -7.~~2~~6 ‰ and *d*-excess = +1~~1.1~~3 ‰).~~

The convective events during ~~representing~~ spring and autumn season exhibited substantially shorter trajectories suggesting that the atmospheric "pump" transporting moisture from the equatorial Atlantic Ocean to the Amazon forest was much weaker or non-existent during this time of the year. Those short trajectories suggest enhanced evapotranspiration of source moisture for rainfall (Salati et al., 1979; Risi et al., 2013; Gat, J. R., & Matsui, 1991; Worden et al., 2007; Brown et al., 2008; Levin et al., 2009; Worden et al., 2021). As a result, those trajectories were characterized by a reduction in the amount of rainfall along the trajectories and enriched $\delta^{18}O_{wgd}$ = ≥ -4.2 ‰$_{wgd}$~~$_{initial}$~~ ~~(≥ -~~4~~3~~.2~~1 ‰)~~ and higher d_{wgd} = ≥ +16.5 ‰. ~~initial~~ weighted average ~~*d*-excess (≥ +1~~6~~0~~.5~~0 ‰).~~

In addition, on 2019/11/05, the highest d_{wgd} (+23.3 ‰) weighted average *d*-excess was observed on 2019/11/05(+23.3 ‰). This was characterized bydue to a continental moisture trajectory circling around Rio Claro (Fig.(Figure 3c) over a greater RH gradient (e.g., sugar cane crop regions)). A possible explanation for the higher *d*-excess value could be evapotranspiration and evaporation from bare soil, such as during the sugarcane crop (da Silva et al., 2021). Evaporation from soil increases kinetic fractionation, favoring the evaporation of HDO due to high diffusivity, resulting in a strong *d*-excess changes (Risi et al., 2013). ~~the highest initial *d*-excess (≥ 24.1 ‰) were observed on 2019/11/05 and 2020/09/06 events. A possible explanation of~~

Formatado: Fonte: Itálico

Formatado: Fonte: Itálico

Formatado: Inglês (Estados Unidos), Verificar ortografia e gramática

Código de campo alterado

Formatado: Inglês (Estados Unidos)

these greater *d*-excess values may be enhanced interaction with the surface of the continent, resulting in evapotranspiration processes. At steady state, transpiration is a non-fractionating process. This means that soil water pumped by plants returns to the atmosphere without any detectable change in its isotopic composition (Cuntz et al., 2007; Flanagan et al., 1991; Dongmann and Nürnberg, 1974). If it is assumed that soil water available to plants has isotopic characteristics equal to the mean values of the two events described, then the water vapor released to the local atmosphere during transpiration will possess identical isotopic signatures. Now, assuming that this water vapor is lifted by convection and then condenses, it is possible to easily calculate the isotopic composition of the first condensate. Assuming an isotopic equilibrium between the gaseous and liquid phases of water in the cloud:

$$\delta_L = \alpha_{eq}(1000 + \delta_V) - 1000 \quad (7)$$

where δ_L and δ_V signify delta values of liquid (condensate) and vapor phase, respectively, at isotopic equilibrium, whereas α_{eq} stands for equilibrium fractionation factor. Equilibrium fractionation factors for ^{2}H, ^{18}O and *d*-excess were calculated using empirical expressions proposed by (Horita and Wesolowski, 1994). The assumed condensation temperature was equal 20 °C and 18 °C (cf. Tdw for 2019/11/05 and 2020/06/09, respectively in Table 1). The calculated isotopic characteristics of the first condensate are equal δ^2H = +85.1 ‰, δ^{18}O = +6.6 ‰, *d*-excess = +32.3 ‰ and δ^2H = +81.0 ‰, δ^{18}O = +6.5 ‰, *d*-excess = +28.8 ‰, for both respectively events. This example calculation suggests the transpiration process could generate isotopically enriched rainfall and greater *d*-excess.

Thus, these regional processes were imprinted in the initial isotopic composition ($\delta^{18}O_{initial}$ and *d*-excess) of all convective events. This regional δ-signature was preserved during summer (2020/01/30 and 2020/02/01), autumn (2020/06/09) and spring (2019/11/05) events, as indicated by similar $\delta^{18}O_{initial}$, $\delta^{18}O_{med}$, lower $\Delta\delta^{18}$O values. In addition, the *d*-excess exhibited greater difference between $\delta_{initial}$ and δ_{med}, and higher δΔ values in relation to the δ^{18}O parameters for all convective rainfall events. The following section provides more detail on the variability of *d*-excess in terms of local atmospheric processes.

Código de campo alterado

Formatado: Recuo: Primeira linha: 0.5 cm

Formatado: Com marcadores, Recuo: Primeira linha: 0 cm

Código de campo alterado

Formatado: Inglês (Estados Unidos)

Formatado: Francês (França)

4.2 Local atmospheric controls

In deep convection, precipitation particles primarily grow through the collection of water (known as coalescence) by larger droplets and/or ice particles (known as riming). These larger particles sweep water from the cloud on their falling paths in the presence of strong rising air currents. Previous studies As a parcel of rising air ascends, the growing particles within it move until they become large enough to fall relative to the air. As the air parcel ascends, particles fall out at each successive height. The remaining lighter particles disperse laterally over a larger area due to the diverging airflow. Convective air movements create concentrated reflectivity peaks in the radar pattern because most of the precipitation mass falls within a few kilometres of the updraft centres (Houghton, 1968; Houze, 1997) noted that in deep precipitation atmospheric convection, the primary growth mechanism for precipitation particles is the collection of water (known as coalescence) from the cloud by larger droplets and/or ice particles (known as riming) that sweep water from the cloud on their falling paths in the presence of strong rising air currents. As a parcel of rising air ascends, the growing particles within it move until they become large enough to fall relative to the air. . The irregular blank bands visible in the vertical MRR profiles (Fig. 5) could be attributed to the lateral dispersion of remaining particles. The concentrated high reflectivity values (Fig. 5) illustrate this pattern, which typically occurs close to the surface and indicates the occurrence of Zmax.

Variations in the isotopic composition of the rainfall reflect changes in this mechanism of raindrop formation (Sun et al., 2022; Aggarwal et al., 2016). This is shown by the vertical variation in the Z values of the events on 2020/02/10, 2021/02/24, 2020/06/09 and 2019/11/05 (grey band in Fig. 6, 7, 8). A possible reason for this change is that the process of coalescence during the falling raindrops towards the surface may have been altered. This can be seen in the higher Zampl values (40 ~ 50 dBZ), which suggest that water particles were being incorporated into the raindrop during the fall at the surface, resulting in a larger water particle and consequently a higher concentration in the raindrops and the occurrence of Zmax close to the surface. The $\delta^{18}O$ values generally increased while the *d*-excess decreased, resulting in a change in the isotopic variation pattern, reflecting the diffusive exchange process between the surrounding vapor and the raindrops As the air parcel grows and floats upwards, particles begin to fall out at each successive height. The remaining particles, which are lighter, are then dispersed laterally over a larger area by the diverging airflow. This lateral spreading is responsible for the irregular blank bands that are visible in the vertical profile of the MRR (Fig. 5i,j-8i,j). Convective air movements produce concentrated reflectivity peaks in the radar pattern due to most of the precipitation mass falling within a few kilometres of the updraft centres. Fig. 5i,j-8i,j illustrate this pattern, which is typically close to the surface, indicating of Zmáx occurrence.

Variations in the isotopic composition of the rainfall reflect changes in this mechanism of raindrop formation (Sun et al., 2022; Aggarwal et al., 2016). This is shown by the vertical variation in the Zc values (including Zmáx, Zmedian and Zamplitude parameters) of the events on 2020/02/10, 2021/02/24, 2020/06/09 and 2019/11/05 (grey band in Fig. 6, 7, 8). A possible reason for this change is that the process of coalescence during the fall of raindrops towards the surface may have been altered. This can be seen in the higher Zamplitude values, which suggest that water particles were being incorporated into the raindrop during the fall at the surface, resulting in a larger water particle and consequently a higher water concentration in the raindrops and the occurrence of Zmáx close to the surface. The $\delta^{18}O$ values generally increased while the *d*-excess decreased, resulting in a change in the isotopic variation pattern, reflecting the diffusive exchange process between the surrounding vapor and the raindrops (Gedzelman and Lawrence, 1990; Celle-Jeanton et al., 2004). In contrast,, since the isotopic pattern of the events on 2020/02/01 (Fig. 5), 2020/01/30 (Fig. 5),RH (~ 90 %). Strong and 2020/05/23 (Fig. 7) exhibited small variation due to the low variability insignificant correlations were found between Z values.parameters and $\delta^{18}O$ and *d*-excess, supporting these findings. Therefore, the main local control on the isotopic variability of intra-events corresponded tois mainly controlled by the vertical structure of the rainfall event..

The *d*-excess values decreased and the $\delta^{18}O$ values increased at the end of the events on 2020/02/01, 2021/02/24 (Fig. 6a) and 2020/02/10 (black dotted cycle in Figs. 5a, 6a and Fig. 6b, respectively). This was due to the formation of residual rainfallrain at low altitudes and a decrease in rainfall intensity during the dissipation phase of the convective cell. On 2020/11/18 (Fig. 8b), the $\delta^{18}O$ values constantly decreased, illustrating a typical depletion of heavy isotopes based on Rayleigh

Formatado: Sobrescrito

Formatado: Fonte: Itálico

Formatado: Sobrescrito

Formatado: Fonte: Itálico

Formatado: Recuo: Primeira linha: 0.5 cm distillation processes due to the progressive condensation of convective systems. Previous studies have widely observed these mechanisms during intra-events, and both interpretations are supported (Adar et al., 1991; Coplen et al., 2008, 2015; Barras and Simmonds, 2009; Celle-Jeanton et al., 2004; Muller et al., 2015).

The events on summer (2020/02/10 and 2021/02/24), autumn (2020/05/23) and spring (2020/11/18) exhibited substantial differences in $\delta_{initial}$, δ_{med}, and higher $\Delta\delta$ for $\delta^{18}O$, $\delta^{2}H$ and *d*-excess (Table 1), implying that local processes modified the regional isotopic imprint.

Overall, the Rayleigh distillation governs the depletion of isotopic composition for the events 2020/02/10 ($^{18}O_{initial}$ = -12.3 ‰ and $\delta^{18}O_{med}$ = -13.9 ‰) and 2020/11/18 ($^{18}O_{initial}$ = -2.7 ‰ and $\delta^{18}O_{med}$ = -4.1 ‰). This depletion is linked to a reduction of isotopic exchange and the local increase in cloud-top heights, which leads to a rise in BT values observed at both events, ranging from -16 to -45 °C (Fig. 5l) and -62 and -65 °C (Fig. 6l), respectively. The intra-event analysis facilitates identification of variable fractionation processes during the evolution of these rainfall systems. The $\delta^{18}O$ trends of both events show similarities, but notable differences in *d*-excess trends occur due to varying vertical profiles and RH conditions. On 2020/02/10, the Zc changed towards the end of the event while RH remained consistently high (97 %). This induced a change in *d*-excess during a specific time of the event. On the other hand, on 2020/11/18, Zc was varied at the beginning of event with lower RH of 70 ~ 82 %, leading to a lower *d*-excess during the start of event. The observed strong and significant correlations between isotopic composition and RH support this variation for both events.

The event of 2021/02/24 provides a suitable example of the impact of local factors. The marked differences between the initial and median values for *d*-excess (13 ‰ and 7.2 ‰, respectively) and the isotopic composition, enriched with initial ($\delta^{18}O_{initial}$ = -7.6 ‰ and $\delta^{2}H_{initial}$ = -47.8 ‰) and median ($\delta^{18}O_{med}$ = -6.8 ‰ and $\delta^{2}H_{med}$ -44.8 ‰) values (Table 1), resulted in a distinctive enrichment in the isotopic composition. This enrichment is associated with the diverse vertical structure of rainfall and low humidity conditions (RH, 78 ~ 88%). Alterations in both rainfall patterns and Zc levels under low humidity conditions promote the preferential escape of lighter isotopologues from liquid water (Dansgaard, 1964). This is corroborated by notable and negative correlations between isotopic composition, rainfall volume, and Zc. In addition, the preferential escape of lighter isotopologues also occurred during the 2020/05/23, characterized by lower RH (78 ~ 89 %), resulted in enriched isotopic composition.

The semi-quantitative evaluation illustrated in Table 2 reinforces the intra-event analysis, suggesting a modification of the mean *d*-excess. The intra-event results indicate that local changes in the isotopic composition of rainfall are controlled by the specific cloud characteristics and the vertical structure of rainfall, which are connected to local humidity conditions. Therefore, the reduction in *d*-excess was greater during the events on 2021/02/24, 2020/05/23, and 2020/11/18 due to cloud features and low humidity conditions, compared to the event on 2020/02/10 that had high local humidity conditions.

5 Concluding remarks

Formatado: Verificar ortografia e gramática

Código de campo alterado

Formatado: Francês (França)

Formatado: Francês (França)

Formatado: Recuo: Primeira linha: 0.5 cm

Formatado: Inglês (Estados Unidos)

ThisThe study usedemployed high-frequency isotopicisotopice composition of rainfall parameters ($\delta_{initial}$, δ_{med}, and $\Delta\delta$) as well as meteorological data to investigate the regional and local mechanisms controlling the isotopic characteristics of convective precipitation.

Based on the inter-event analysis, it has been revealed that the regional isotopic characteristics are different between summer and autumn-spring seasons. The $\delta_{wgd wgd initial}$ is determined by moisture transport mechanisms and convection features. The mainkey factors are the gradual reduction of heavy isotopes progressive rainfall along moisture trajectories. The rainfall produced and Rayleigh distillation along these tracks was the moisture transport pathway. The effect of rainfall along trajectories is pronounced during summer events, associated with the longer moisture transport pathway from the Amazon Forest, producingforest, which produces depleted isotope valuesheavy isotopes. In contrast, reduced autumn and spring rainfall along trajectories isare associated with athe shorter moisture transport pathway from the Atlantic Ocean and southern Brazil. This produces , producing enriched isotope characteristics and high d_{wgd} values . This regional δ-signature has been preserved in both summer, autumn, and spring events. Specific events in autumn and spring with high *d*-excess values were associated with transpirationevapotranspiration and soil evaporation of soil processes along the moisture transport pathway.

Within ., demonstrating how regional convective events,processes interact with the tropical surface and alter the isotopic composition.

During the advance of convective rainfall, the regional δ_{wgd}δ-signature was altered by local effects, generated the isotope variability (large Δδ values), as shown by the intra-event isotopic evolution.evaluation. The vertical structure of rainfall, describedas shown by the Z parameters in the vertical MRR profile and Z parameters, is the main local control. During falling raindrops, a microphysical change can cause a vertical change in Z values, resulting in abrupt variations in isotopic patterns. These findingsThese changes were observed in all Z parameters (maximum, median, and amplitude) and were supported by significant and strong correlations between the MRR parameters and isotopic parameters in each event. The critical local controls are the cloud changes and the vertical structure of the rainfall. The local controls occur under certain specific conditions of low relative humidity of ambient. These local mechanisms amplify the discrepancy between the $\delta_{initial}$ and δ_{med} values, leading to significant Δδ values. Significant correlations between $\delta^{18}O$, *d*-excess, Zc, and RH, as well as the semi-quantitative evaluation, lend support to the significance of the vertical structure and relative humidity conditions outlined in this study.

Therefore, the isotopic composition of convective rainfall is controlled by an interplay of regional and local factors. The complex and dynamic conditions of convective rainfall formation across the tropics can be understood using high-frequency analysis. Although high-frequency rainfall sampling is logistically difficult, we encourage future studies of this type in different geographical regions across the tropics, to better understand the factors controlling the isotopic composition of convective rainfall during rainy period. Extensive monitoring of local meteorological parameters and modeling of regional moisture transport to the rainfall collection site, along with the application of more robust below-cloud models, should accompany such studies.

~~Through identifying the complexity of the factors that make up the isotopic composition of convective rainfall in the study area, it was possible to understand why it was so difficult to apply regression models in past studies when using daily data and separation of rainfall types for the Rio Claro GNIP station.~~

~~Although high-frequency rainfall sampling is logistically difficult, we encourage future studies of this type in different geographical regions across the tropics, to better understand the factors controlling the isotopic composition of convective rainfall during rainy period. Extensive monitoring of local meteorological parameters and modeling of regional moisture transport to the rainfall collection site, along with the application of more robust below-cloud models, should accompany such studies.~~

Formatado: Recuo: Primeira linha: 0 cm

Data availability

A complete database (isotope characteristics of rainfall as well as selected meteorological parameters characterizing these events) are available at: https://doi.org/10.17632/kk3gs8zn4s.1 (dos Santos et al., 2023). Monthly GNIP data: https://www.iaea.org/services/networks/gnip. GOES-16 imageries are available at: https://home.chpc.utah.edu/~u0553130/Brian_Blaylock/cgi-bin/goes16_download.cgi. The weather systems are available at: https://www.marinha.mil.br/chm/dados-do-smm-cartas-sinoticas/cartas-sinoticas and http://tempo.cptec.inpe.br/boletimtecnico/pt. Reanalysis data are available at: (https://cds.climate.copernicus.eu/cdsapp#!/search?type=dataset. The Global Modeling and Assimilation Office (GMAO) data are available at: https://goldsmr4.gesdisc.eosdis.nasa.gov/data/MERRA2/M2T1NXFLX.5.12.4/). Goddard Earth Sciences Data and Information Services Center (GES DISC) data are available at: https://disc.gsfc.nasa.gov/datasets/AIRS3STD_7.0/summary.

Acknowledgment

FAPESP support for the scholarship provided under the Process 2019/03467-3 and 2021/10538-4 is acknowledged. Durán-Quesada acknowledges time for analysis and writing provided within UCR C1038 project. The authors acknowledge Troy G. for English revision.

Financial support

This work was funded by grants the São Paulo Research Foundation (FAPESP) under Processes 2018/06666-4, 2019/03467-3 and 2021/10538-4, and by the International Atomic Energy Agency Grant CRP-F31006.

References

Adar, E. M. ., Karnieli, A. ., Sandler, B. Z. ., Issar, A. ., Wolf, M. ., and Landsman, L.: A mechanical sequential rain sampler for isotopic and chemical analysis, Vienna, 32 pp., 1991.

Adler, R. F. and Fenn, D. D.: Thunderstorm vertical velocities estimated from satellite data, American, 36, 1747–1754, https://doi.org/10.1175/1520-0469(1979)036,1747: TVVEFS.2.0.CO;2., 1979.

Adler, R. F. and Mack, R. A.: Thunderstorm cloud top dynamics as inferred from satellite observations and a cloud top parcel model, American Meteorological Society, 43, 1945–1960, https://doi.org/10.1175/ 1520-0469(1986)043,1945:TCTDAI.2.0.CO;2, 1986.

Aemisegger, F. ., Spiegel, J. K. ., Pfahl, S. ., Sodemann, H. ., Eugster, W. ., and Wernli, H.: Isotope meteorology of cold front passages: A case study combining observations and modeling, Geophysical Research Letters, 42, 5652–5660, https://doi.org/10.1002/2015GL063988, 2015.

Aggarwal, P. K., Romatschke, U., Araguas-Araguas, L., Belachew, D., Longstaffe, F. J., Berg, P., Schumacher, C., and Funk, A.: Proportions of convective and stratiform precipitation revealed in water isotope ratios, Nature Geoscience, 9, 624–629, https://doi.org/10.1038/ngeo2739, 2016.

Barras, V. and Simmonds, I.: Observation and modeling of stable water isotopes as diagnostics of rainfall dynamics over southeastern Australia, Journal of Geophysical Research Atmospheres, 114, https://doi.org/10.1029/2009JD012132, 2009.

Bony, S., Risi, C., and Vimeux, F.: Influence of convective processes on the isotopic composition (δ 18 O and δ D) of precipitation and water vapor in the tropics: 1. Radiative-convective equilibrium and Tropical Ocean–Global Atmosphere–Coupled Ocean-Atmosphere Response Experiment (TOGA-CO, Journal of Geophysical Research: Atmospheres, 113, 1–21, https://doi.org/10.1029/2008JD009942, 2008.

Breugem, A. J., Wesseling, J. G., Oostindie, K., and Ritsema, C. J.: Meteorological aspects of heavy precipitation in relation to floods – An overview, Earth-Science Reviews, 204, 103171, https://doi.org/10.1016/j.earscirev.2020.103171, 2020.

Brown, D., Worden, J., and Noone, D.: Comparison of atmospheric hydrology over convective continental regions using water vapor isotope measurements from space, Journal of Geophysical Research: Atmospheres, 113, 1–17, https://doi.org/10.1029/2007JD009676, 2008.

Celle-Jeanton, H., Gonfiantini, R., Travi, Y., and Sol, B.: Oxygen-18 variations of rainwater during precipitation: Application of the Rayleigh model to selected rainfalls in Southern France, Journal of Hydrology, 289, 165–177, https://doi.org/10.1016/j.jhydrol.2003.11.017, 2004.

Coplen, T. B., Neiman, P. J., White, A. B., Landwehr, J. M., Ralph, F. M., and Dettinger, M. D.: Extreme changes in stable hydrogen isotopes and precipitation characteristics in a landfalling Pacific storm, Geophysical Research Letters, 35, L21808, https://doi.org/10.1029/2008GL035481, 2008.

Coplen, T. B., Neiman, P. J., White, A. B., Ralph, F. M., Coplen, T. B., Neiman, P. J., White, A. B., and Ralph, F. M.: Tellus B : Chemical and Physical Meteorology Categorisation of northern California rainfall for periods with and without a radar brightband using stable isotopes and a novel automated precipitation collector Categorisation of northern California rainfall , 0889, https://doi.org/10.3402/tellusb.v67.28574, 2015.

Dansgaard, W.: Stable isotopes in precipitation, Tellus, 16, 436–468, https://doi.org/10.3402/tellusa.v16i4.8993, 1964.

Donat, M. G., Alexander, L. V., Yang, H., Durre, I., Vose, R., Dunn, R. J. H., Willett, K. M., Aguilar, E., Brunet, M., Caesar, J., Hewitson, B., Jack, C., Klein Tank, A. M. G., Kruger, A. C., Marengo, J., Peterson, T. C., Renom, M., Oria Rojas, C., Rusticucci, M., Salinger, J., Elrayah, A. S., Sekele, S. S., Srivastava, A. K., Trewin, B., Villarroel, C., Vincent, L. A., Zhai, P., Zhang, X., and Kitching, S.: Updated analyses of temperature and precipitation extreme indices since the beginning of the twentieth century: The HadEX2 dataset, Journal of Geophysical Research Atmospheres, 118, 2098–2118, https://doi.org/10.1002/jgrd.50150, 2013.

Endries, J. L., Perry, L. B., Yuter, S. E., Seimon, A., Andrade-Flores, M., Winkelmann, R., Quispe, N., Rado, M., Montoya, N., Velarde, F., and Arias, S.: Radar-observed characteristics of precipitation in the tropical high andes of Southern Peru and Bolivia, Journal of Applied Meteorology and Climatology, 57, 1441–1458, https://doi.org/10.1175/JAMC-D-17-0248.1, 2018.

van der Ent, R. J. and Tuinenburg, O. A.: The residence time of water in the atmosphere revisited, Hydrology and Earth System Sciences, 21, 779–790, https://doi.org/10.5194/hess-21-779-2017, 2017.

Froehlich, K., Gibson, J. J., and Aggarwal, P.: Deuterium excess in precipitation and its climatological significance, Journal of Geophysical Research-Atmospheres, 1–23, 2002.

Gadgil, S.: The Indian monsoon and its variability, Annual Review of Earth and Planetary Sciences, 31, 429–467, https://doi.org/10.1146/annurev.earth.31.100901.141251, 2003.

Galewsky, J., Schneider, M., Diekmann, C., Semie, A., Bony, S., Risi, C., Emanuel, K., and Brogniez, H.: The influence of convective aggregation on the stable isotopic composition of water vapor, AGU Advances, 4, 1–16, https://doi.org/10.1029/2023AV000877, 2023.

García-Santos, S., Sánchez-Murillo, R., Peña-Paz, T., Chirinos-Escobar, M. J., Hernández-Ortiz, J. O., Mejía-Escobar, E. J., and Ortega, L.: Water stable isotopes reveal a complex rainfall to groundwater connectivity in central Honduras, Science of the Total Environment, 844, https://doi.org/10.1016/j.scitotenv.2022.156941, 2022.

Garreaud, R. D.: Cold air incursions over subtropical South America: Mean structure and dynamics, Monthly Weather Review, 128, 2544–2559, https://doi.org/10.1175/1520-0493(2000)128<2544:caioss>2.0.co;2, 2000.

Gat, J. R., & Matsui, E.: Atmospheric water balance in the Amazon Basin: An isotopic evapotranspiration model, Journal of Geophysical Research, 96, 13179–13188, https://doi.org/https://doi.org/10.1029/91JD00054, 1991.

Gedzelman, S. D. and Lawrence, J. R.: The Isotopic Composition of Precipitatin from Two Extratropical Cyclones, American Meteorological Society, 118, 495–509, https://doi.org/10.1175/1520-0493(1990)118,0495: TICOPF.2.0.CO;2, 1990.

Gimeno, L., Drumond, A., Nieto, R., Trigo, R. M., and Stohl, A.: On the origin of continental precipitation, Geophysical Research Letters, 37, 1–7, https://doi.org/10.1029/2010GL043712, 2010.

Gimeno, L., Vázquez, M., Eiras-Barca, J., Sorí, R., Stojanovic, M., Algarra, I., Nieto, R., Ramos, A. M., Durán-Quesada, A. M., and Dominguez, F.: Recent progress on the sources of continental precipitation as revealed by moisture transport analysis, Earth-Science Reviews, 201, 103070, https://doi.org/10.1016/j.earscirev.2019.103070, 2020.

Graf, P., Wernli, H., Pfahl, S., and Sodemann, H.: A new interpretative framework for below-cloud effects on stable water isotopes in vapour and rain, Atmospheric Chemistry and Physics, 19, 747–765, https://doi.org/10.5194/acp-19-747-2019, 2019.

Han, X., Lang, Y., Wang, T., Liu, C.-Q., Li, F., Wang, F., Guo, Q., Li, S., Liu, M., Wang, Y., and Xu, A.: Temporal and spatial variations in stable isotopic compositions of precipitation during the typhoon Lekima (2019), China, Science of The Total Environment, 762, 143143, https://doi.org/10.1016/j.scitotenv.2020.143143, 2021.

Houghton, H. G.: On Precipitation Mechanisms and their Artificial Modification, Journal of Applied Meteorology, 7, 851–859, https://doi.org/10.1175/1520-0450(1968)007<0851:OPMATA>2.0.CO;2, 1968.

Houze, R.: Stratiform precipitation in regions of convection: A Meteorological Paradox?, Bulletin of the American Meteorological Society, 78, 2179–2195, 1997.

Houze, R. A.: Cloud dynamics, Academic Press Limited, 573 pp., https://doi.org/10.1016/0377-0265(87)90017-0, 1993.

Houze, R. A.: Mesoscale Convective Systems, in: International Geophysics, vol. 104, 237–286, https://doi.org/10.1016/B978-0-12-374266-7.00009-3, 2004.

Houze, R. A. J.: Observed structure of mesoscale convective systems and implications for large-scale heating., Quart. J. Roy. Meteor. Soc., 115, 425–461, 1989.

IAEA: IAEA / GNIP precipitation sampling guide V2.02, Global Network of Isotopes in Precipitation (GNIP), 20, 2014.

IPCC, W. G. I.-T. P. S. B.: Regional fact sheet – Central and South America, Sixth Assessment Report, 1–2 pp., 2021.

Jeelani, G., Deshpande, R. D., Galkowski, M., and Rozanski, K.: Isotopic composition of daily precipitation along the southern foothills of the Himalayas: Impact of marine and continental sources of atmospheric moisture, Atmospheric Chemistry and Physics, 18, 8789–8805, https://doi.org/10.5194/acp-18-8789-2018, 2018.

Kastman, J., Market, P., Fox, N., Foscato, A., and Lupo, A.: Lightning and rainfall characteristics in elevated vs. surface based convection in the midwest that produce heavy rainfall, Atmosphere, 8, 36, https://doi.org/10.3390/atmos8020036, 2017.

Klaassen, W.: Radar Observations and Simulation of the Melting Layer of Precipitation, Journal of the Atmospheric Sciences, 45, 3741–3753, 1988.

Kodama, Y.: Large-scale common features of subtropical precipitation zones (the Baiu Frontal Zone , the SPCZ , and the SACZ) Part I: Characteristics of subtropical frontal zones, Journal of the Meteorological Society of Japan, 70, 813–836, https://doi.org/10.1248/cpb.37.3229, 1992.

Kurita, N.: Water isotopic variability in response to mesoscale convective system over the tropical ocean, Journal of Geophysical Research Atmospheres, 118, 10376–10390, https://doi.org/10.1002/jgrd.50754, 2013.

Kurita, N., Ichiyanagi, K., Matsumoto, J., Yamanaka, M. D., and Ohata, T.: The relationship between the isotopic content of precipitation and the precipitation amount in tropical regions, Journal of Geochemical Exploration, 102, 113–122, https://doi.org/10.1016/j.gexplo.2009.03.002, 2009.

Lacour, J. L., Risi, C., Worden, J., Clerbaux, C., and Coheur, P. F.: Importance of depth and intensity of convection on the isotopic composition of water vapor as seen from IASI and TES δD observations, Earth and Planetary Science Letters, 481, 387–394, https://doi.org/10.1016/j.epsl.2017.10.048, 2018.

Landais, A., Agosta, C., Vimeux, F., Magand, O., Solis, C., Cauquoin, A., Dutrievoz, N., Risi, C., Leroy-Dos Santos, C., Fourré, E., Cattani, O., Jossoud, O., Minster, B., Prié, F., Casaso, M., Dommergue, A., Bertrand, Y., and Werner, M.: Abrupt excursion in water vapor isotopic variability during cold fronts at the Pointe Benedicte observatory in Amsterdam Island, Atmospheric Chemistry and Physics, Preprint, 1–33, https://doi.org/https://doi.org/10.5194/egusphere-2023-1617, 2023.

Lawrence, J. R., Gedzelman, S. D., Dexheimer, D., Cho, H., Carrie, G. D., Gasparini, R., Anderson, C. R., Bowman, K. P., and Biggerstaff, M. I.: Stable isotopic composition of water vapor in the tropics, Journal of Geophysical Research: Atmospheres, 109, 16, https://doi.org/10.1029/2003JD004046, 2004.

Lee, J. and Fung, I.: "Amount effect" of water isotopes and quantitative analysis of post-condensation processes, Hydrological Processes, 22, 1–8, https://doi.org/10.1002/hyp.6637, 2008.

Lekshmy, P. R., Midhun, M., Ramesh, R., and Jani, R. A.: 18 O depletion in monsoon rain relates to large scale organized convection rather than the amount of rainfall, Scientific Reports, 4, 1–5, https://doi.org/10.1038/srep05661, 2014.

Levin, N. E., Zipser, E. J., and Ceding, T. E.: Isotopic composition of waters from Ethiopia and Kenya: Insights into moisture sources for eastern Africa, Journal of Geophysical Research Atmospheres, 114, 1–13, https://doi.org/10.1029/2009JD012166, 2009.

Lima, K. C., Satyamurty, P., and Fernández, J. P. R.: Large-scale atmospheric conditions associated with heavy rainfall episodes in Southeast Brazil, Theoretical and Applied Climatology, 101, 121–135, https://doi.org/10.1007/s00704-009-0207-9, 2010.

Luiz Silva, W., Xavier, L. N. R., Maceira, M. E. P., and Rotunno, O. C.: Climatological and hydrological patterns and verified trends in precipitation and streamflow in the basins of Brazilian hydroelectric plants, Theoretical and Applied Climatology, 137, 353–371, https://doi.org/10.1007/s00704-018-2600-8, 2019.

Machado, L. A. T. and Rossow, W. B.: Structural Characteristics and Radiative Properties of Tropical Cloud Clusters, Monthly Weather Review, 121, 3234–3260, 1993.

Machado, L. A. T., Rossow, W. B., Guedes, R. L., and Walker, A. W.: Life cycle variations of mesoscale convective systems over the Americas, Monthly Weather Review, 126, 1630–1654, https://doi.org/10.1175/1520-0493(1998)126<1630:LCVOMC>2.0.CO;2, 1998.

Marengo, J. A., Soares, W. R., Saulo, C., and Nicolini, M.: Climatology of the low-level jet east of the Andes as derived from the NCEP-NCAR reanalyses: Characteristics and temporal variability, Journal of Climate, 17, 2261–2280, https://doi.org/10.1175/1520-0442(2004)017<2261:COTLJE>2.0.CO;2, 2004.

Marengo, J. A., Ambrizzi, T., Alves, L. M., Barreto, N. J. C., Simões Reboita, M., and Ramos, A. M.: Changing Trends in Rainfall Extremes in the Metropolitan Area of São Paulo: Causes and Impacts, Frontiers in Climate, 2, 1–13, https://doi.org/10.3389/fclim.2020.00003, 2020.

Marengo, J. A., Camarinha, P. I., Alves, L. M., Diniz, F., and Betts, R. A.: Extreme Rainfall and Hydro-Geo-Meteorological Disaster Risk in 1.5, 2.0, and 4.0°C Global Warming Scenarios: An Analysis for Brazil, Frontiers in Climate, 3, 1–17, https://doi.org/10.3389/fclim.2021.610433, 2021.

Mehta, S., Mehta, S. K., Singh, S., Mitra, A., Ghosh, S. K., and Raha, S.: Characteristics of the Z–R Relationships Observed

Using Micro Rain Radar (MRR-2) over Darjeeling (27.05° N, 88.26° E): A Complex Terrain Region in the Eastern Himalayas, Pure and Applied Geophysics, 177, 4521–4534, https://doi.org/10.1007/s00024-020-02472-6, 2020.

Moerman, J. W., Cobb, K. M., Adkins, J. F., Sodemann, H., Clark, B., and Tuen, A. A.: Diurnal to interannual rainfall δ18O variations in northern Borneo driven by regional hydrology, Earth and Planetary Science Letters, 369–370, 108–119, https://doi.org/10.1016/j.epsl.2013.03.014, 2013.

Muller, C. L., Baker, A., Fairchild, I. J., Kidd, C., and Boomer, I.: Intra-Event Trends in Stable Isotopes: Exploring Midlatitude Precipitation Using a Vertically Pointing Micro Rain Radar, Journal of Hydrometeorology, 16, 194–213, https://doi.org/10.1175/JHM-D-14-0038.1, 2015.

Munksgaard, N. C., Kurita, N., Sánchez-Murillo, R., Ahmed, N., Araguas, L., Balachew, D. L., Bird, M. I., Chakraborty, S., Kien Chinh, N., Cobb, K. M., Ellis, S. A., Esquivel-Hernández, G., Ganyaglo, S. Y., Gao, J., Gastmans, D., Kaseke, K. F., Kebede, S., Morales, M. R., Mueller, M., Poh, S. C., Santos, V. dos, Shaoneng, H., Wang, L., Yacobaccio, H., and Zwart, C.: Data Descriptor: Daily observations of stable isotope ratios of rainfall in the tropics, Scientific Reports, 9, 1–7, https://doi.org/10.1038/s41598-019-50973-9, 2019.

R Core Team: A language and environment for statistical computing. R Foundation for Statistical Computing, Vienna, Austria. https://www.R-project.org/., 2023.

Rao, N. T., Kirankumar, N. V. P., Radhakrishna, B., and Rao, N. D.: Classification of tropical precipitating systems using wind profiler spectral moments. Part I: Algorithm description and validation, Journal of Atmospheric and Oceanic Technology, 25, 884–897, https://doi.org/10.1175/2007JTECHA1031.1, 2008.

Ribeiro, B. Z., Machado, L. A. T., Biscaro, T. S., Freitas, E. D., Mozer, K. W., and Goodman, S. J.: An evaluation of the GOES-16 rapid scan for nowcasting in southeastern brazil: Analysis of a severe hailstorm case, Weather and Forecasting, 34, 1829–1848, https://doi.org/10.1175/WAF-D-19-0070.1, 2019.

Risi, C., Bony, S., and Vimeux, F.: Influence of convective processes on the isotopic composition (δ18O and δD) of precipitation and water vapor in the tropics: 2. Physical interpretation of the amount effect, Journal of Geophysical Research Atmospheres, 113, 1–12, https://doi.org/10.1029/2008JD009943, 2008.

Risi, C., Bony, S., Vimeux, F., Chongd, M., and Descroixe, L.: Evolution of the stable water isotopic composition of the rain sampled along sahelian squall lines, Quarterly Journal of the Royal Meteorological Society, 136, 227–242, https://doi.org/10.1002/qj.485, 2010.

Risi, C., Noone, D., Frankenberg, C., and Worden, J.: Role of continental recycling in intraseasonal variations of continental moisture as deduced from model simulations and water vapor isotopic measurements, Water Resources Research, 49, 4136–4156, https://doi.org/10.1002/wrcr.20312, 2013.

Roberts, R. D. and Rutledge, S.: Nowcasting storm initiation and growth using GOES-8 and WSR-88D data, Weather and Forecasting, 18, 562–584, https://doi.org/10.1175/1520-0434(2003)018<0562:NSIAGU>2.0.CO;2, 2003.

Roca, R. and Fiolleau, T.: Extreme precipitation in the tropics is closely associated with long-lived convective systems, Communications Earth & Environment, 1, 18, https://doi.org/10.1038/s43247-020-00015-4, 2020.

Romatschke, U. and Houze, R. A.: Characteristics of precipitating convective systems accounting for the summer rainfall of tropical and subtropical South America, Journal of Hydrometeorology, 14, 25–46, https://doi.org/10.1175/JHM-D-12-060.1, 2013.

Rozanski, K., Sonntag, C., and Munnich, K. O.: Factors controlling stable isotope composition of European precipitation., Tellus, 34, 142–150, https://doi.org/10.3402/tellusa.v34i2.10796, 1982.

Rozanski, K., Araguás-Araguás, L., and Gonfiantini, R.: Isotopic Patterns in Modern Global Precipitation, 1–36, https://doi.org/10.1029/GM078p0001, 1993.

Salati, E., Dall'Olio, A., Matsui, E., and Gat, J. R.: Recycling of water in the Amazon Basin: An isotopic study, Water Resources Research, 15, 1250–1258, https://doi.org/10.1029/WR015i005p01250, 1979.

Sánchez-Murillo, R., Durán-Quesada, A. M., Birkel, C., Esquivel-Hernández, G., and Boll, J.: Tropical precipitation anomalies and d-excess evolution during El Niño 2014-16, Hydrological Processes, 31, 956–967, https://doi.org/10.1002/hyp.11088, 2017.

Sánchez-Murillo, R., Durán-Quesada, A. M., Esquivel-Hernández, G., Rojas-Cantillano, D., Birkel, C., Welsh, K., Sánchez-Llull, M., Alonso-Hernández, C. M., Tetzlaff, D., Soulsby, C., Boll, J., Kurita, N., and Cobb, K. M.: Deciphering key processes controlling rainfall isotopic variability during extreme tropical cyclones, Nature Communications, 10, 1–10, https://doi.org/10.1038/s41467-019-12062-3, 2019.

dos Santos, V., Gastmans, D., and Sánchez-Murillo, R.: Isotope and meteorologic database of high-frequency sampling of convective rainfall events in Rio Claro, Brazil, https://doi.org/10.17632/kk3gs8zn4s.1, 2023.

Schmit, T. J., Griffith, P., Gunshor, M. M., Daniels, J. M., Goodman, S. J., and Lebair, W. J.: A closer look at the ABI on the goes-r series, Bulletin of the American Meteorological Society, 98, 681–698, https://doi.org/10.1175/BAMS-D-15-00230.1, 2017.

Shapiro, S. S.; Wilk, M. B.: An analysis of variance test for normality (complete samples), Biometrika, 53, 591–611, 1965.

da Silva, G. J., Berg, E. C., Calijuri, M. L., dos Santos, V. J., Lorentz, J. F., and Carmo Alves, S. do: Aptitude of areas planned for sugarcane cultivation expansion in the state of São Paulo, Brazil: a study based on climate change effects, Agriculture, Ecosystems & Environment, 305, 107164, https://doi.org/10.1016/j.agee.2020.107164, 2021.

Siqueira, J. R. and Machado, L. A. T.: Influence of the frontal systems on the day-to-day convection variability over South America, Journal of Climate, 17, 1754–1766, https://doi.org/10.1175/1520-0442(2004)017<1754:IOTFSO>2.0.CO;2, 2004.

Siqueira, J. R., Rossow, W. B., Machado, L. A. T., and Pearl, C.: Structural characteristics of convective systems over South America related to cold-frontal incursions, Monthly Weather Review, 133, 1045–1064, https://doi.org/10.1175/MWR2888.1, 2005.

Soderberg, K., Good, S. P., O'connor, M., Wang, L., Ryan, K., and Caylor, K. K.: Using atmospheric trajectories to model the isotopic composition of rainfall in central Kenya, Ecosphere, 4, 1–18, https://doi.org/10.1890/ES12-00160.1, 2013.

Stein, A. F., Draxler, R. R., Rolph, G. D., Stunder, B. J. B., Cohen, M. D., and Ngan, F.: Noaa's hysplit atmospheric transport and dispersion modeling system, Bulletin of the American Meteorological Society, 96, 2059–2077, https://doi.org/10.1175/BAMS-D-14-00110.1, 2015.

Steiner, M. and Smith, J. A.: Convective versus stratiform rainfall: An ice-microphysical and kinematic conceptual model, Atmospheric Research, 47–48, 317–326, https://doi.org/10.1016/S0169-8095(97)00086-0, 1998.

Sun, C., Shanahan, T. M., and Partin, J.: Controls on the Isotopic Composition of Precipitation in the South-Central United States, Journal of Geophysical Research: Atmospheres, 124, 8320–8335, https://doi.org/10.1029/2018JD029306, 2019.

Sun, C., Tian, L., Shanahan, T. M., Partin, J. W., Gao, Y., Piatrunia, N., and Banner, J.: Isotopic variability in tropical cyclone precipitation is controlled by Rayleigh distillation and cloud microphysics, Communications Earth & Environment, 3, https://doi.org/10.1038/s43247-022-00381-1, 2022.

Taupin, J.-D., Gallaire, R., and Arnaud, Y.: Analyses isotopiques et chimiques des précipitations sahélienne de la région de Niamey au Niger: implications climatologiques, Hydrochemistry, 151–162, 1997.

Thurnherr, I. and Aemisegger, F.: Disentangling the impact of air – sea interaction and boundary layer cloud formation on stable water isotope signals in the warm sector of a Southern Ocean cyclone, Atmospheric Chemistry and Physics, 22, 10353–10373, https://doi.org/10.5194/acp-22-10353-2022, 2022.

Torri, G.: On the Isotopic Composition of Cold Pools in Radiative-Convective Equilibrium, Journal of Geophysical Research: Atmospheres, 126, 1–20, https://doi.org/10.1029/2020JD033139, 2021.

Tremoy, G., Vimeux, F., Soumana, S., Souley, I., Risi, C., Favreau, G., and Oï, M.: Clustering mesoscale convective systems with laser-based water vapor δ 18 O monitoring in Niamey (Niger), Journal of Geophysical Research: Atmospheres, 119, 5079–5103, https://doi.org/10.1002/2013JD020968, 2014.

Uijlenhoet, R.: Raindrop size distributions and radar reflectivity–rain rate relationships for radar hydrology, Hydrology and Earth System Sciences, 5, 615–628, https://doi.org/10.5194/hess-5-615-2001, 2001.

Vila, D. A., Machado, L. A. T., Laurent, H., and Velasco, I.: Forecast and tracking the evolution of cloud clusters (ForTraCC) using satellite infrared imagery: Methodology and validation, Weather and Forecasting, 23, 233–245, https://doi.org/10.1175/2007WAF2006121.1, 2008.

de Vries, A. J., Aemisegger, F., Pfahl, S., and Wernli, H.: Stable water isotope signals in tropical ice clouds in the West African monsoon simulated with a regional convection-permitting model, Atmospheric Chemistry and Physics, 22, 8863–8895, https://doi.org/10.5194/acp-22-8863-2022, 2022.

Worden, J., Noone, D., Bowman, K., Beer, R., Eldering, A., Fisher, B., Gunson, M., Goldman, A., Herman, R., Kulawik, S. S., Lampel, M., Osterman, G., Rinsland, C., Rodgers, C., Sander, S., Shephard, M., Webster, C. R., and Worden, H.: Importance of rain evaporation and continental convection in the tropical water cycle, Nature, 445, 528–532, https://doi.org/10.1038/nature05508, 2007.

Worden, S., Fu, R., Chakraborty, S., Liu, J., and Worden, J.: Where Does Moisture Come From Over the Congo Basin?, Journal of Geophysical Research: Biogeosciences, 126, 1–14, https://doi.org/10.1029/2020JG006024, 2021.

World Meteorological Organization: WMO Atlas of Mortality and Economic Losses From Weather , Climate and Water Extremes (1970-2019), Geneva 2, Switzerland, 90 pp., 2021.

Formatado: Francês (França), Verificar ortografia e

Zilli, M. T., Carvalho, L. M. V., Liebmann, B., and Silva Dias, M. A.: A comprehensive analysis of trends in extreme precipitation over southeastern coast of Brazil, International Journal of Climatology, 37, 2269–2279, https://doi.org/10.1002/joc.4840, 2017.
Zwart, C., Munksgaard, N. C., Protat, A., Kurita, N., Lambrinidis, D., and Bird, M. I.: The isotopic signature of monsoon conditions, cloud modes, and rainfall type, Hydrological Processes, 32, 2296–2303, https://doi.org/10.1002/hyp.13140, 2018.

Table 1. Summarizing overall convective rainfall events, isotope and meteorological parameters

Season		Spring		Autumn		Summer			
Data		05/11/2019	18/11/2020	09/06/2020	23/05/2020	30/01/2020	10/02/2020	01/02/2020	24/02/2021
Number of samples		21	8	12	4	6	18	5	16
Duration		82	141	96	131	23	86	18	55
$\delta^{18}O$	Median	-3.1	-4.2	-3.4	-2.9	-10.0	-13.9	-10.4	-6.8
	Weighted average	-3.0	-4.2	-2.7	-2.9	-10.0	-13.4	-11.1	-7.2
$\delta^{2}H$	Median	0.8	-13.7	-5.6	-6.9	-64.4	-92.0	-73.5	-44.8
	Weighted average	-1.2	-14.9	-4.9	-6.8	-63.9	-90.4	-75.0	-47.2
d-excess	Median	22.9	19.7	17.3	16.3	15.7	17.5	13.4	7.2
	Weighted average	23.3	19.1	17.3	16.5	16.5	16.7	14.2	11.1
Automatic Weather Station	Rain rate	0.4	0.2	0.3	0.0	0.4	0.5	0.6	0.5
	RH	96	86	95	87	93	97	93	86
	T	21	20	19	19	23	22	23	21
	Tdw	20	17	18	17	21	21	21	18
	LCL	146	489	168	449	247	93	253	468
Micro Rain Radar	Z	46	38	42	33	38	41	39	35
	w	8	7.1	7.7	6.6	6.6	6.7	7.1	7.1
GOES-16	BT	-63	-63	-50	-56	-53	-39	-60	-51

Season		Spring		Autumn		Summer			
Data		2019/11/05	2020/11/18	2020/05/23	2020/06/09	2020//01/30	2020/02/10	2020/02/01	2021/02/24
Number of samples		21	8	4	12	6	18	5	16
Duration		82	141	131	96	23	86	18	55
$\delta^{18}O$	Initial	-3.0	-2.7	-2.6	-3.6	-10.1	-12.3	-10.2	-7.6
	Median	-3.1	-4.2	-2.9	-3.4	-10	-13.9	-10.4	-6.8
	Δδ	2.4	2.6	0.8	2.2	1.1	7.3	1.5	3.5
$\delta^{2}H$	Initial	3.4	-4.6	-4.6	-5.2	-60.1	-86.6	-71.0	-47.8
	Median	0.8	-13.7	-6.9	-5.6	-64.4	-92.0	-73.5	-44.8
	Δδ	16.9	9.9	8.9	11	10.5	43.1	7.4	20.9
d-excess	Initial	27.4	10.2	16.7	24.1	20.8	12.1	11.3	13.0

Tabela format

Tabela format

	Median	22.9	19.7	16.3	17.3	15.7	17.5	13.4	7.2
	Δδ	7.1	12.8	4.0	19.2	9.5	16.6	8.4	17.2
Automatic Weather Station	Rain rate	0.4	0.2	0.1	0.3	0.4	0.5	0.6	0.5
	RH	96	85	87	95	93	97	93	86
	T	21	20	19	19	23	22	23	21
	Tdw	20	17	17	18	21	21	21	18
	LCL	146	489	449	168	247	93	253	468
Micro Rain Radar	Zc	46	38	33	42	38	41	39	35
	w	8	7.1	6.6	7.7	6.6	6.7	7.1	7.1
GOES-16	BT	-63	-63	-56	-50	-53	-39	-60	-51

905 Duration (minutes); Isotopes parameters (‰); Median values of meteorological variables: Rain rate (mm.min^{-1}), Relative Humidity – (RH %), Temperature (T °C), Dew Temperature (Tdw °C), Lifting Condensation Level (LCL meters), Reflectivity (ZZc dBZ), Vertical Velocity (m.s^{-1}) and Brightness temperature (BT °C).

Table 2. The results of semi-quantitative assessment of the impact of below-cloud processes on the isotope characteristics of convective precipitation

Rainfall event	**T_{INT} a) (°C)**	**RH_{INT} b) (%)**	**F c) (-)**	**Δ d-excess d) (‰)**
The 2019/11/05 event δ_o – isotopic composition of rainfall (‰): δ^2H = 0.80, $\delta^{18}O$ = −3.11, *d*-excess = 25.7 δ_A – isotopic composition of equilibrium vapour (‰) e): δ^2H = −78.3 $\delta^{18}O$ = −12.84, *d*-excess = 24.4	19.3	97.8	0.9982	1.7
The 2020/11/18 δ_o – isotopic composition of rainfall (‰): δ^2H = -13.7, $\delta^{18}O$ = -4.16, *d*-excess = 19.5 δ_A – isotopic composition of equilibrium vapour (‰): δ^2H = −93.2 $\delta^{18}O$ = −14.01, *d*-excess = 18.8	19.0	92.9	0.9795	3.1
The 2020/05/23 δ_o – isotopic composition of rainfall (‰): δ^2H = −6.9, $\delta^{18}O$ = −2.89, *d*-excess = 16.2 δ_A – isotopic composition of equilibrium vapour (‰): δ^2H = −86.6 $\delta^{18}O$ = −12.72, *d*-excess = 15.2	18.1	93.4	0.9806	2.8
The 2020/06/09 δ_o – isotopic composition of rainfall (‰): δ^2H = −5.5, $\delta^{18}O$ = −3.37, *d*-excess = 21.3 δ_A – isotopic composition of equilibrium vapour (‰): δ^2H = −84.8 $\delta^{18}O$ = −13.15, *d*-excess = 20.4	19.3	97.5	0.9978	0.2
The 2020/01/30 δ_o – isotopic composition of rainfall (‰): δ^2H = -64.4, $\delta^{18}O$ = -10.03, *d*-excess = 15.8 δ_A – isotopic composition of equilibrium vapour (‰) e): δ^2H = −135.5 $\delta^{18}O$ = −19.44, *d*-excess = 20.0	22.4	96.4	0.9944	0.9
The 2020/02/10 δ_o – isotopic composition of rainfall (‰): δ^2H = −91.97, $\delta^{18}O$ = −13.85, *d*-excess = 18.8 δ_A – isotopic composition of equilibrium vapour (‰) e): δ^2H = −161.6 $\delta^{18}O$ = −23.28, *d*-excess = 24.6	21.7	98.6	0.9994	0.1
The 2020/02/01 δ_o – isotopic composition of rainfall (‰): δ^2H = −73.5, $\delta^{18}O$ = −10.44, *d*-excess = 10.2 δ_A – isotopic composition of equilibrium vapour (‰) e): δ^2H = −143.8 $\delta^{18}O$ = −19.80, *d*-excess = 14.6	22.5	96.3	0.9947	0.9
The 2021/02/24 δ_o – isotopic composition of rainfall (‰): δ^2H = −44.8, $\delta^{18}O$ = −6.79, *d*-excess = 9.5 δ_A – isotopic composition of equilibrium vapour (‰): δ^2H = −120.3 $\delta^{18}O$ = −16.48, *d*-excess = 11.5	19.3	93.2	0.9800	3.0

a) mean temperature of below cloud ambient atmosphere (linear interpolation between cloud base and ground level values)

b) mean relative humidity of below cloud ambient atmosphere (linear interpolation between cloud base and ground level values)
c) remaining mass fraction of raindrops after their travel from the cloud base to the surface (see text)
d) reduction of the *d*-excess of raindrops as a result of their travel from the cloud base to the surface (see text)
e) assumed isotopic composition of ambient humid atmosphere below the cloud base derived from the measured isotopic composition of rainfall and ground-level temperature.

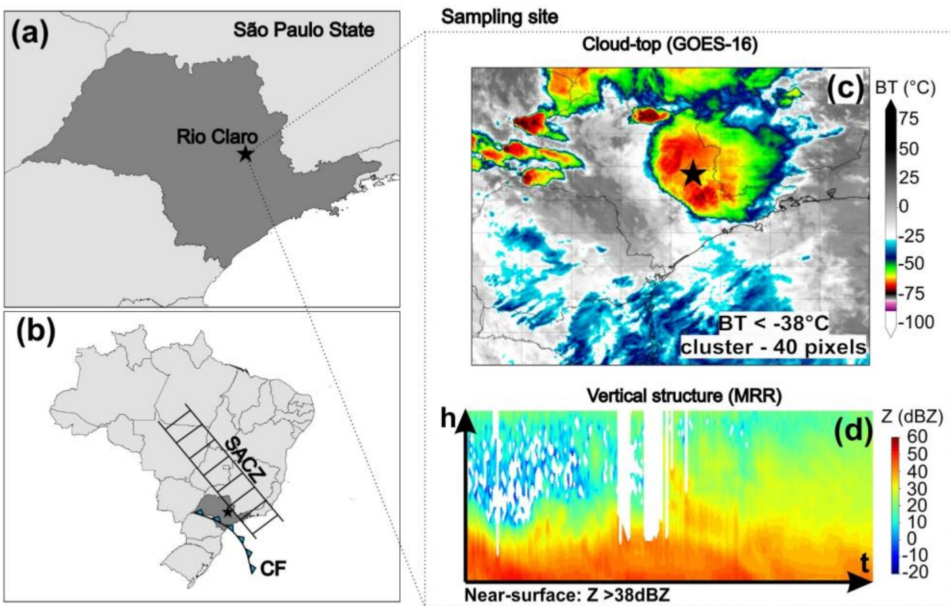

Figure 1. Regional and local context of study area. (a) Localization of sampling site in Rio Claro (black star) (b) regional synoptic context across Brazil and main weather systems (CF – cold front and SACZ – Southern Atlantic Convergence Zone). (c) GOES-16 satellite imagery of convective rainfall (d) Micro Rain Radar (MRR) image of convective rainfall.

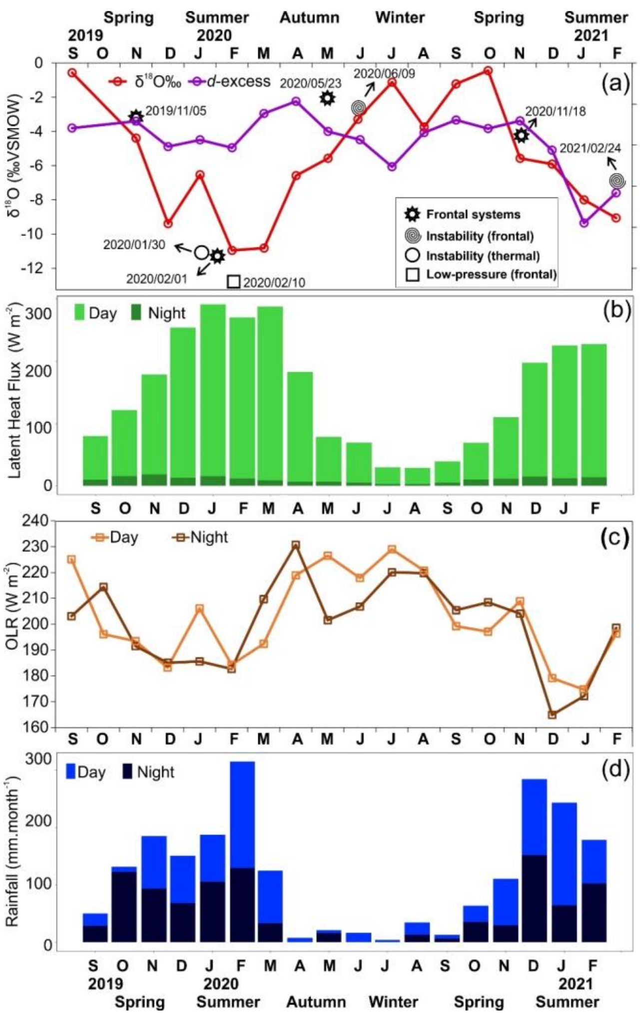

Figure 2. Seasonal variation of isotope and convective parameters. (a) Temporal distribution of monthly $\delta^{18}O$ and *d*-excess values during study period, with aggregated median of $\delta^{18}O$ values for high-frequency convective rainfall events (b) AQUA/AIRS latent heat flux. (c) MERRA-2 outgoing longwave radiation (monthly averaged daytime and night-time data) (d) monthly rainfall amounts at Rio Claro separated into day and night fraction (no rainfall types distinguished). The black symbol indicates weather systems described in section 3.1. The monthly isotopic composition used in this figure was collected by the first authors of the article and determined by the UNESP laboratory, following the same procedures mentioned in section 2.2.

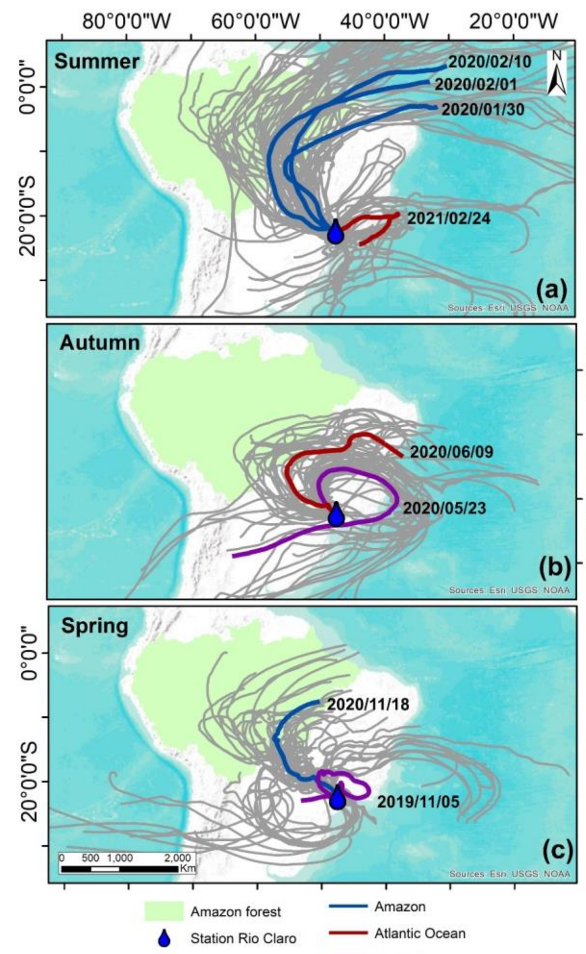

Figure 3. Ten-day backward trajectories arriving at Rio Claro station of eight convective events. (a) Summer, (b) Autumn and (c) Spring. Twenty-seven ensembles are grey lines, and the mean trajectory is the colors lines. The colours of the mean trajectories indicate the origin of air masses. The authors used trivial information, the borders of the countries and the ocean provided by the ESRI base map.

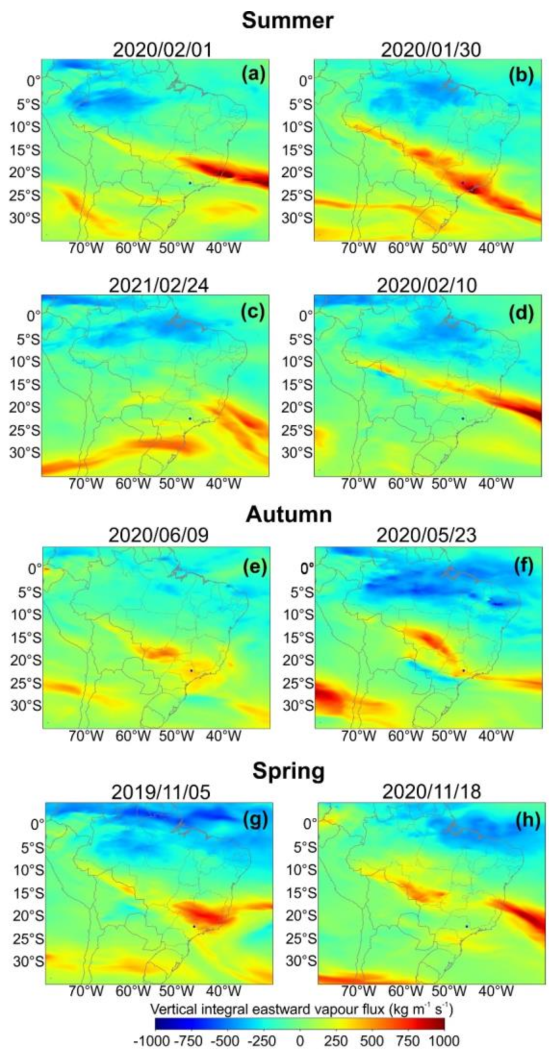

Figure 4. ERA-5 vertical integral of eastward water vapor flux. (a, b, c, d) summer convective events (e, f) autumn and (g, h) spring aggregated. The maps corresponded to the days when convective rainfall events occurred. Positive values indicate the direction of moisture vapor flux from left to right, and negative values from right to left.

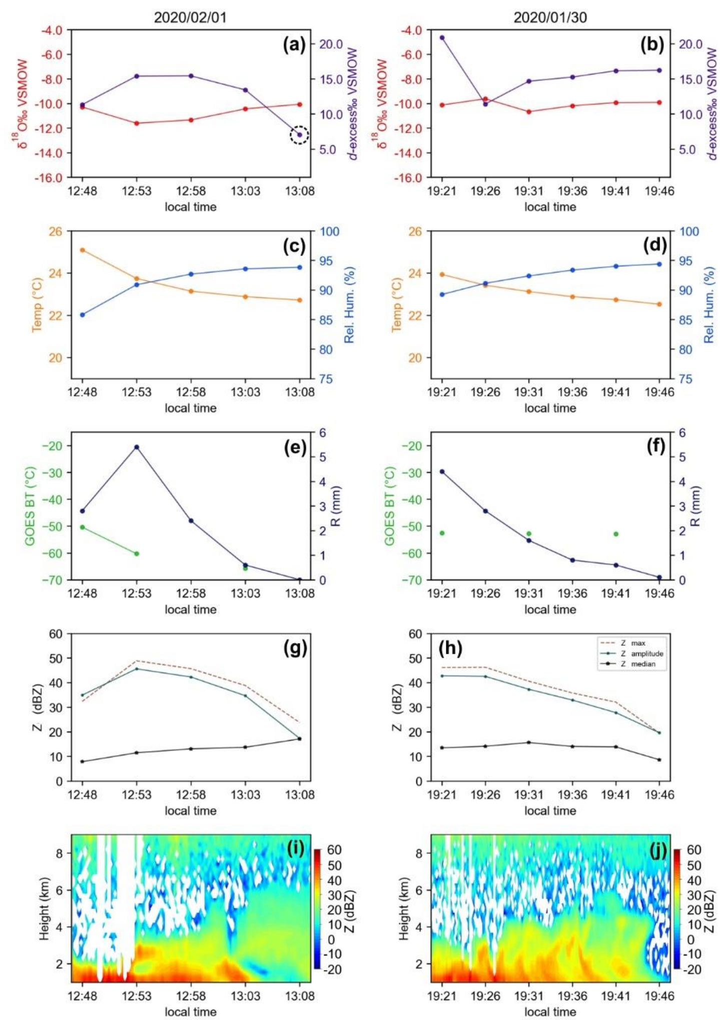

2020/02/01
2020/01/30
(a)
(b)
(c)
(d)
(e)
(f)
(g)
(h)
(i)
(j)
δ18O‰ VSMOW
d-excess‰ VSMOW
Temp (°C)
Rel. Hum. (%)
GOES BT (°C)
R (mm)
Z (dBZ)
Z max
Z amplitude
Z median
Height (km)
local time

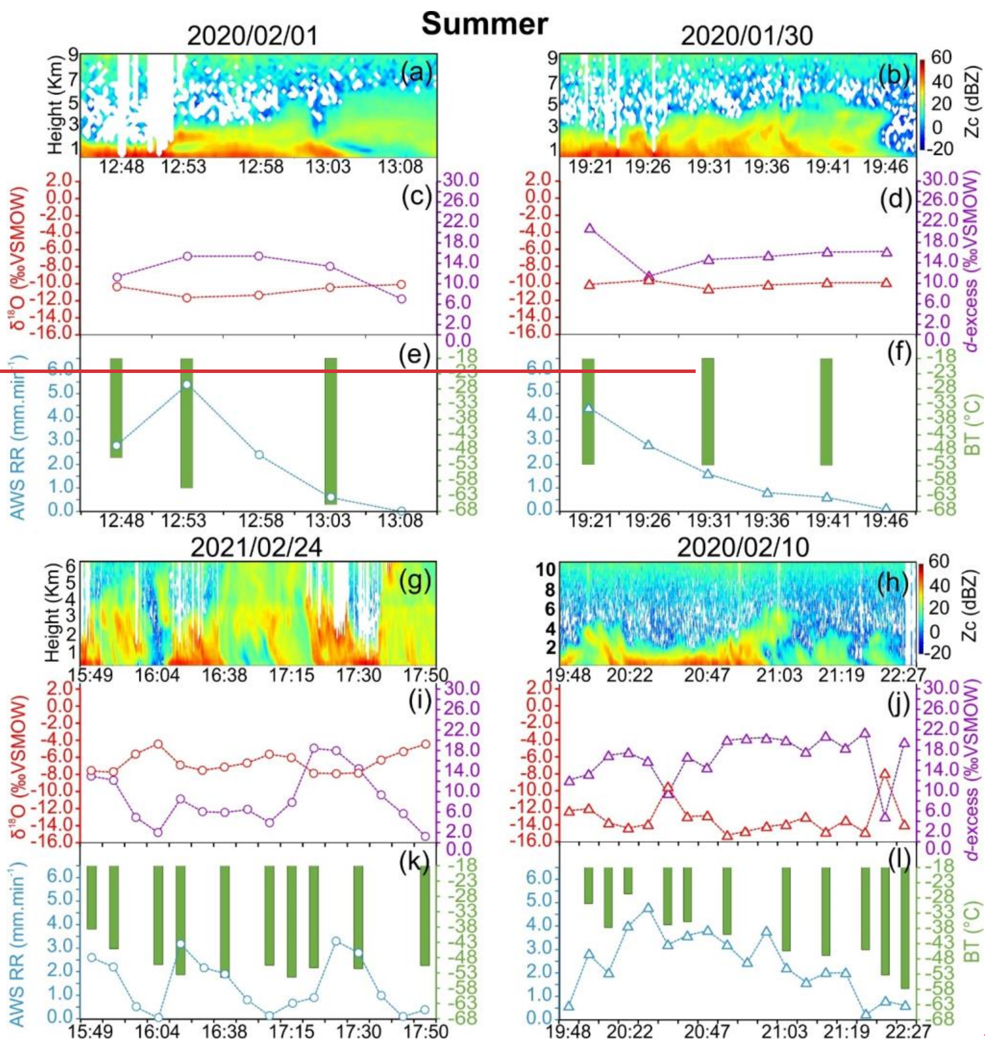
Summer
2020/02/01
2020/01/30
2021/02/24
2020/02/10
(a)
(b)
(c)
(d)
(e)
(f)
(g)
(h)
(i)
(j)
(k)
(l)
Height (Km)
Zc (dBZ)
δ18O (‰VSMOW)
d-excess (‰VSMOW)
AWS RR (mm.min-1)
BT (°C)

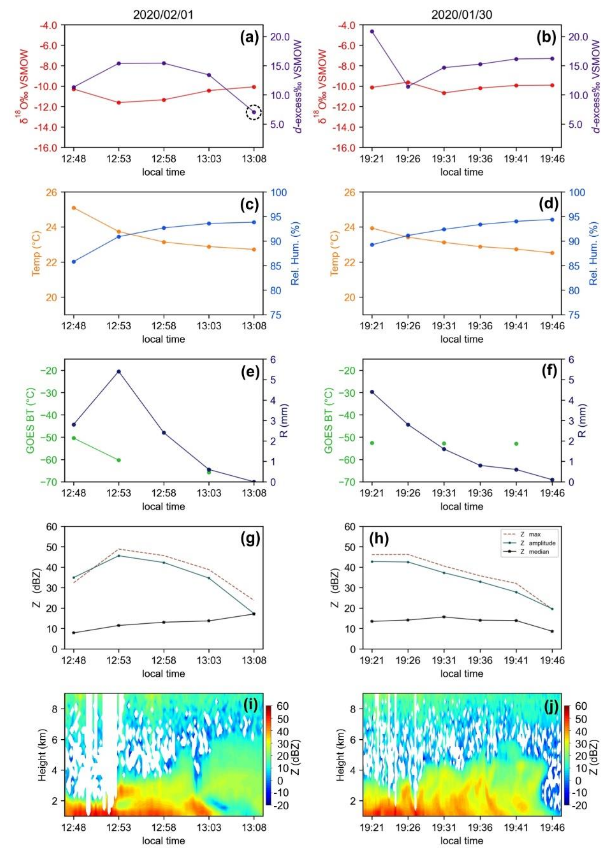

Figure 5. Summer intra-events. (a(a, b, g, h) radar reflectivity of Micro Rain Radar (c, d, i, ja, b) δ^{18}O (red lines) and *d*-excess (purple lines) (c, d) Temperature (orange lines) and Relative Humidity (blue lines) (e, f, k, l) brightness temperature (BT – green bars) and rainfall amount (blue lines) (g, h) Reflectivity parameters, ZZc maximum (red lines), ZZc amplitude (green lines) and ZZc median (black lines) (i, j) radar reflectivity of Micro Rain Radar. The black dotted cycle refers to the low *d*-excess value. .

Formatado: Inglês (Estados Unidos)

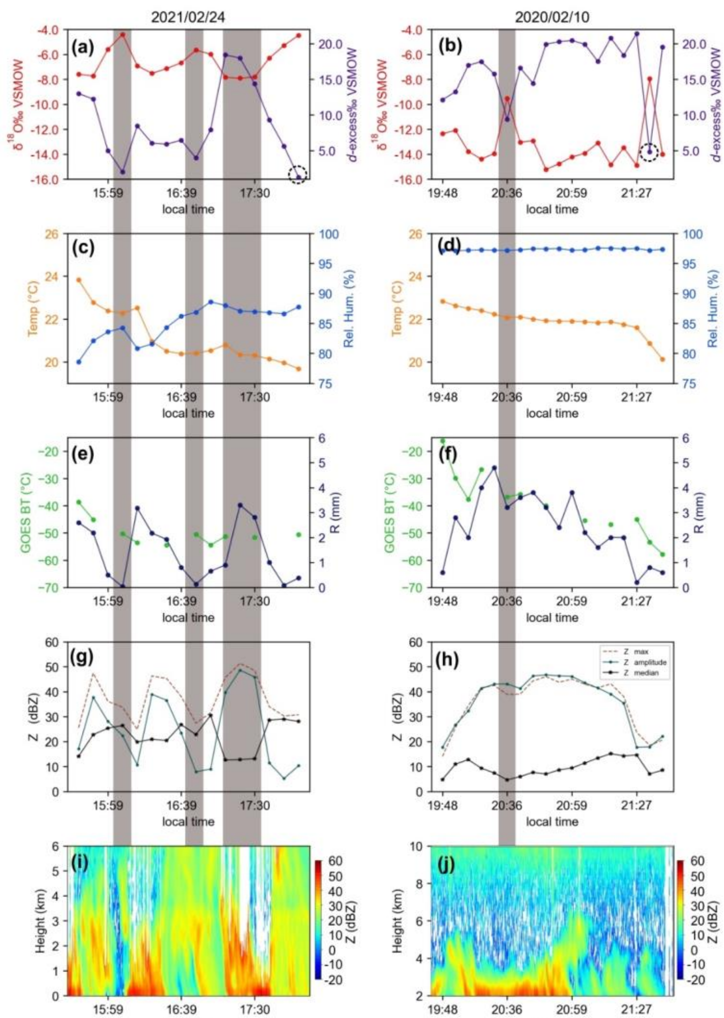

2021/02/24
2020/02/10
(a)
(b)
δ18O‰ VSMOW
d-excess‰ VSMOW
(c)
(d)
Temp (°C)
Rel. Hum. (%)
(e)
(f)
GOES BT (°C)
R (mm)
(g)
(h)
Z (dBZ)
Z max
Z amplitude
Z median
(i)
(j)
Height (km)
Z (dBZ)
local time
15:59
16:39
17:30
19:48
20:36
20:59
21:27

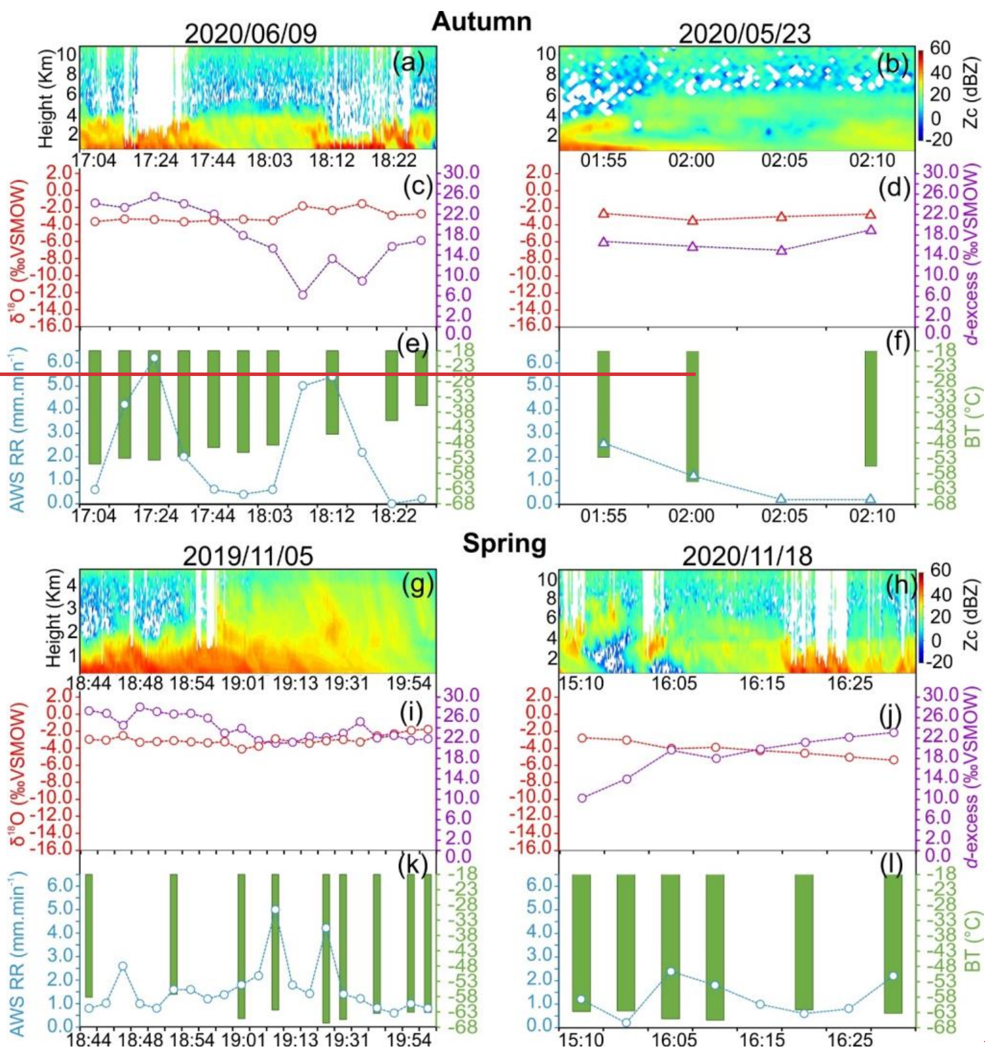

Autumn
2020/06/09
2020/05/23
(a)
(b)
(c)
(d)
(e)
(f)
Height (Km)
Zc (dBZ)
δ18O (‰VSMOW)
d-excess (‰VSMOW)
AWS RR (mm.min-1)
BT (°C)
17:04
17:24
17:44
18:03
18:12
18:22
01:55
02:00
02:05
02:10
Spring
2019/11/05
2020/11/18
(g)
(h)
(i)
(j)
(k)
(l)
18:44
18:48
18:54
19:01
19:13
19:31
19:54
15:10
16:05
16:15
16:25

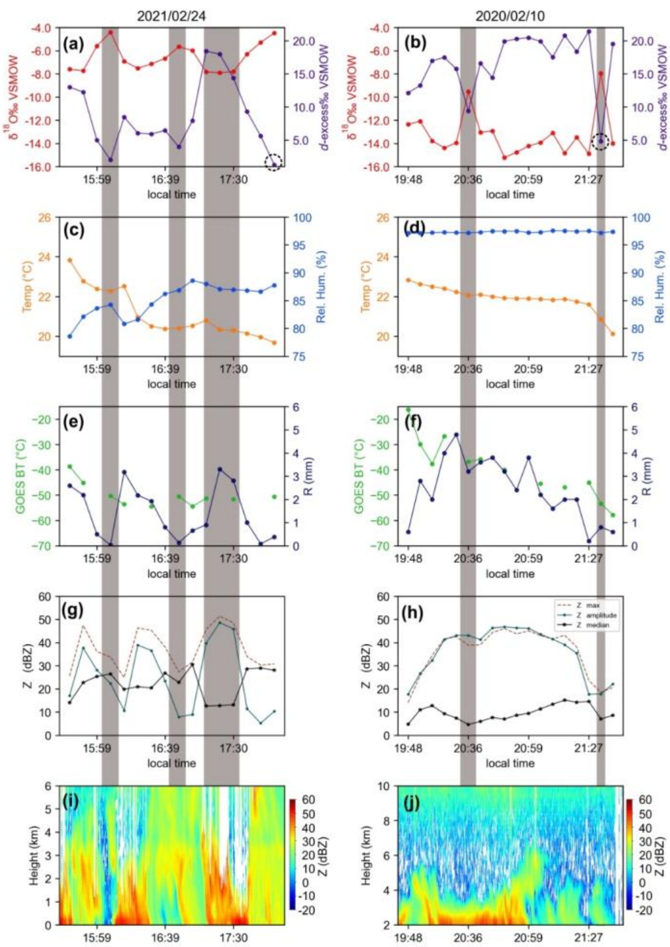

Figure 6. Summer~~Autumn and spring~~Summer intra-events. Refer to Fig. 5 for legend description.

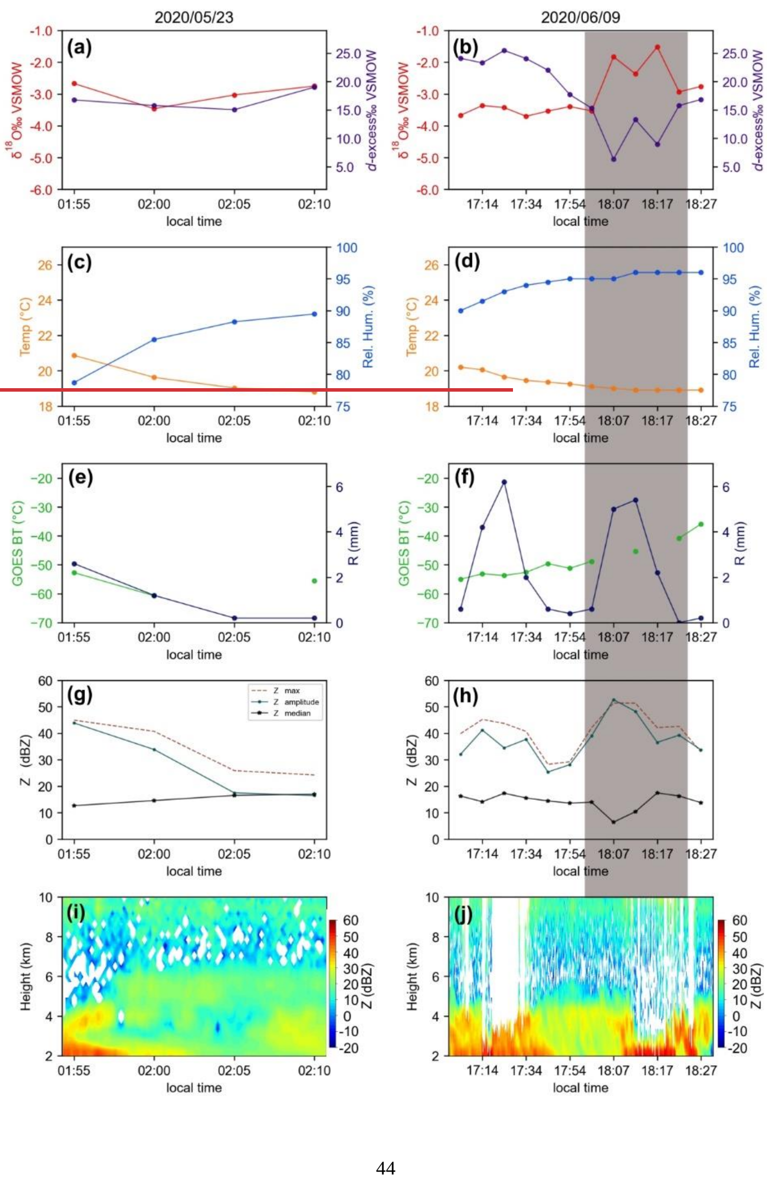
2020/05/23
2020/06/09
(a)
(b)
(c)
(d)
(e)
(f)
(g)
(h)
(i)
(j)
δ18O‰ VSMOW
d-excess‰ VSMOW
Temp (°C)
Rel. Hum. (%)
GOES BT (°C)
R (mm)
Z (dBZ)
Z max
Z amplitude
Z median
Height (km)
Z (dBZ)
local time

965

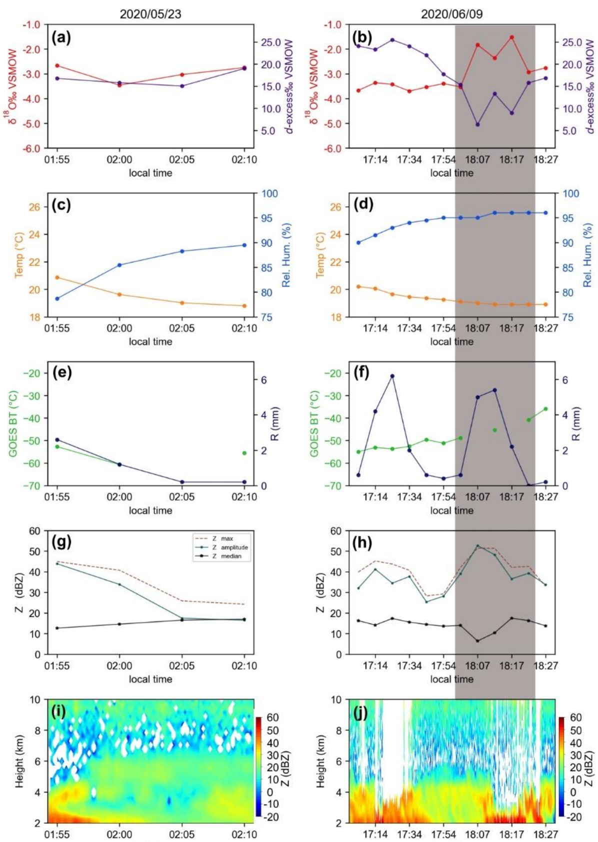

Figure 7. Autumn intra-events. Refer to Fig. 5 for legend description.

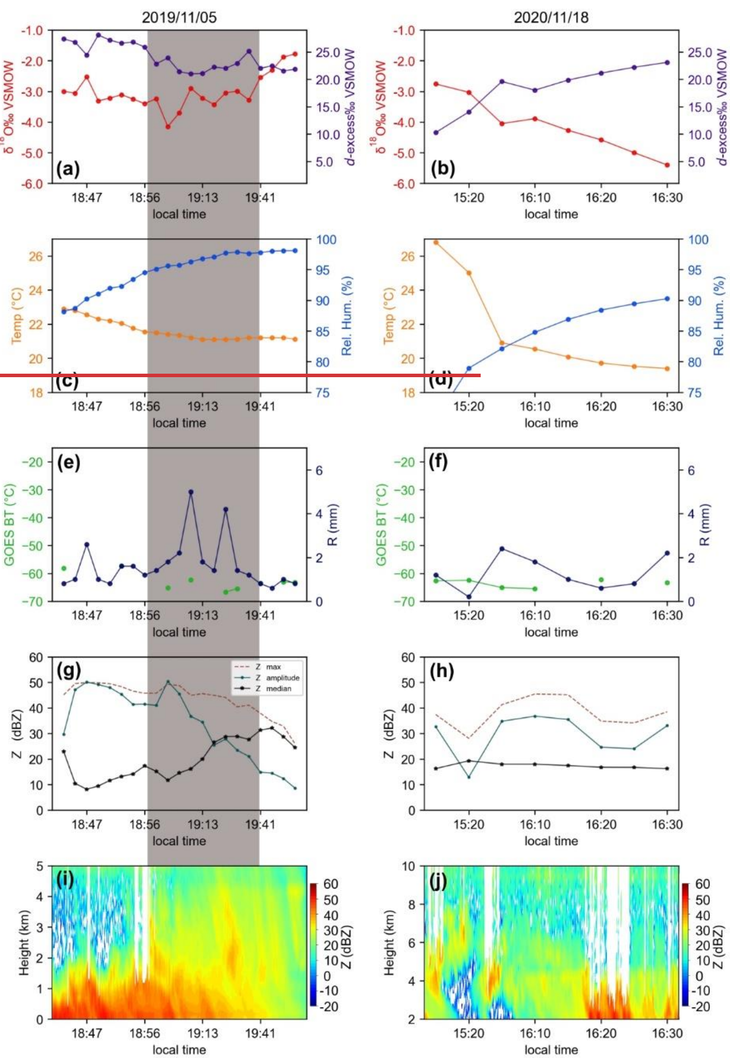
2019/11/05
2020/11/18
δ18O‰ VSMOW
d-excess‰ VSMOW
(a)
(b)
local time
Temp (°C)
Rel. Hum. (%)
(c)
(d)
GOES BT (°C)
R (mm)
(e)
(f)
Z (dBZ)
Z max
Z amplitude
Z median
(g)
(h)
Height (km)
Z (dBZ)
(i)
(j)

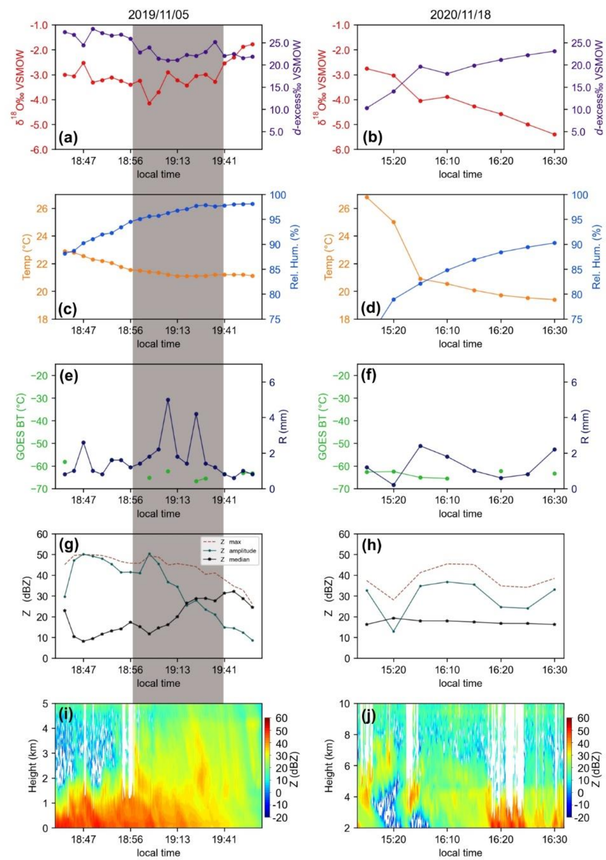

Figure 8. Spring intra-events. Refer to Fig. 5 for legend description.